The following article appeared in Journal of Volcanology and Geothermal Research Volume 443, November 2023, 107920 and may be found at: https://doi.org/10.1016/j.jvolgeores.2023.107920

Journal of Volcanology and Geothermal Research 443 (2023) 107920

Contents lists available at ScienceDirect

Journal of Volcanology and Geothermal Research

journal homepage: www.journals.elsevier.com/journal-of-volcanology-and-geothermal-research

Alternating Subplinian and phreatomagmatic phases during the construction of a phonolitic maar-diatreme volcano (Caldera del Rey, Tenerife, Canary Islands)

Oliver Bowers [a], Pablo Dávila Harris [b], Rebecca Winstanley [a], Fabian B. Wadsworth [a], Richard J. Brown [a,*]

[a] Department of Earth Sciences, Durham University, Durham DH1 3LE, UK
[b] División de Geociencias Aplicadas, IPICYT, San Luis Potosí 78216, Mexico

ARTICLE INFO

Keywords:
Maar-diatreme
Phreatomagmatism
Pyroclastic density current
Subplinian
Tenerife

ABSTRACT

The Early Pleistocene, well exposed, Caldera del Rey maar-diatreme volcano, Tenerife, Canary Islands was constructed during a ~ VEI 4 phonolitic eruption that involved two cycles of magmatic-to-phreatomagmatic activity and resulted in two overlapping craters aligned NE-SW. Magmatic phases fed unsteady Subplinian eruption columns that reached 8–12 km altitude and dispersed tephra to the west and southwest of the volcano and shed pyroclastic density currents. Phreatomagmatic phases, driven by explosive interactions between magma and groundwater, constructed an extensive tephra ring via deposition from ballistic curtains, pyroclastic density currents, and tephra fall. Near-optimal-scaled depth phreatomagmatic explosions (strong and/or shallow) excavated a substantial diatreme beneath the north crater and constructed a substantial tephra ring. This abruptly transitioned to deeper-than-optimal scaled depth explosions (weak and/or deep) that erupted mostly fine ash which was dispersed by dilute pyroclastic density currents and fallout and filled the south crater. At distances of >4 km from the volcano, over a metre of ash and pumice accumulated during the phreatomagmatic phases. The Caldera del Rey volcano provides an instructive study on how interaction between ascending felsic magma and groundwater can modify Subplinian eruptions.

1. Introduction

Phreatomagmatic volcanoes such as maars, tuff rings, and tuff cones account for between 0 and 70% of volcanoes that make up monogenetic basaltic fields (Lorenz, 1986; White and Ross, 2011; Brown and Valentine, 2013; Graettinger, 2018). There are numerous published descriptions of these volcanoes and their deposits (e.g., Kienle et al., 1980; Kokelaar, 1983; Chough and Sohn, 1990; Sohn and Chough, 1989; White, 1991; Sohn, 1996; Cole et al., 2001; Freda et al., 2005; Carrasco-Núñez et al., 2007; Solgevik et al., 2007; Valentine et al., 2015; Sweeney et al., 2018; El Messbahi et al., 2020; Tchamabé et al., 2020; Aziwo et al., 2022; Valentine et al., 2022). Those fed by silicic magmas are less common (e.g., Sieh and Bursik, 1986; Brooker et al., 1993; Brown et al., 2007; Cano-Cruz and Carrasco-Núñez, 2008; Tait et al., 2009; Austin-Erickson et al., 2011; Zimmer et al., 2010; Monsalve et al., 2023), but maars and tuff rings share many features with mafic types, including geometry and structure of the volcanic edifice, lithology, grainsize, and bedding characteristics of the deposits, the abundance of ash aggregates and evidence for wet deposition of tephra, and numerous ballistic clasts (Ross et al., 2017).

The rarity of silicic phreatomagmatic volcanoes reflects primarily the lower frequency of eruptions of silicic magma, but also differences between mafic and silicic eruptions, such as the viscosity of the magma and typical mass eruption rates. Low viscosities and low mass eruption rates of mafic magmas favour explosive interactions between magma and ground or surface water (Heiken and Wohletz, 1987; Wohletz and Heiken, 1992; Austin-Erickson et al., 2008). The high viscosity of silicic magmas is thought to inhibit the formation of hydrodynamic premixes of magma and water — a key initial step in triggering phreatomagmatic explosions (Heiken and Wohletz, 1987; Wohletz and Heiken, 1992; Austin-Erickson et al., 2008). Experiments suggest that stress-induced fracturing of silicic melts can allow sufficient contact between magma and water to drive explosions (Austin-Erickson et al., 2008). This process would be most efficient in degassed, low magma flux batches of silicic

* Corresponding author.
E-mail address: Richard.Brown3@durham.ac.uk (R.J. Brown).

https://doi.org/10.1016/j.jvolgeores.2023.107920
Received 29 November 2022; Received in revised form 3 August 2023; Accepted 27 September 2023
Available online 6 October 2023

magma (Ross et al., 2017).

Field studies, experimental work and numerical modelling have profoundly changed our understanding of maar-diatreme volcanism over the past decade (Valentine and White, 2012; Graettinger et al., 2014; Sonder et al., 2015; Valentine et al., 2015; Valentine et al., 2017). Experimental and numerical studies have revealed the importance of the concept of scaled depth for diatreme-hosted phreatomagmatic explosions. Scaled depth, $D_{sc} = d \times E^{-1/3}$ relates the physical depth of an explosion, d, to the mechanical energy released by the explosion, E, and has units of $m.J^{-1/3}$ (Houser, 1969; Goto et al., 2001; Graettinger et al.,

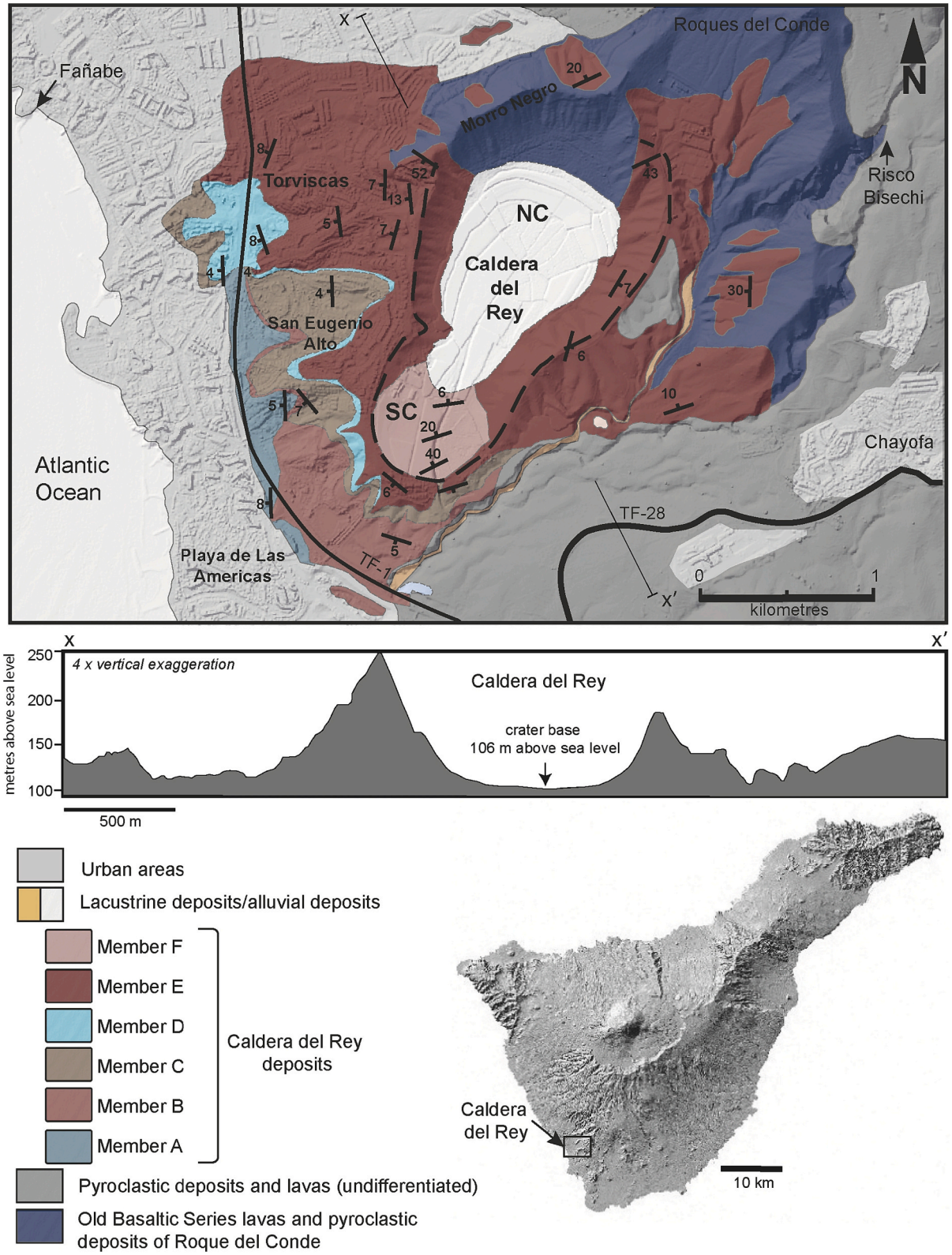

Fig. 1. Geological map of Caldera del Rey. Inset: location of Caldera del Rey on Tenerife. NC – north crater; SC - south crater. Elevation data for cross-section from Google Earth © 2021. Digital Terrain Model courtesy of visor.grafcan.es/visorweb [COLOUR].

2014; Valentine et al., 2014). Explosions in a diatreme propel material around and above the explosion site towards the surface via debris jets (McClintock and White, 2006). The scaled depth of the explosion dictates, in part, the volume and grainsize of material that erupts at the surface, along with the nature of any cratering. Experiments have constrained the optimal scaled depth for crater formation to 0.004 $m.J^{-1/3}$. This results in the greatest volume of ejecta for a given energy. At scaled depth values of >0.008 $m.J^{-1/3}$ (deeper-than-optimal scaled depth) the explosion is confined and ejecta does not breach the surface (Goto et al., 2001; Graettinger et al., 2014; Valentine et al., 2014). At intermediate scaled depth values, only fine-grained material breaches the surface. Explosions may occur at any depth within a diatreme and variably contribute to the growth of the diatreme and the tephra ring (Valentine et al., 2017). Explosions at near-optimal scaled depth produce eruptive jets that collapse and expand outwards as ballistic curtains, i.e., ejected particles move collectively as dispersions with ballistic trajectories (Graettinger et al., 2015). The deposits of experimentally produced ballistic curtains are poorly sorted, massive, of variable thickness and pass outwards into sheet-like deposits (Graettinger et al., 2014). This experimental work has also expanded understanding of how PDCs are generated during maar-diatreme forming eruptions. Alongside collapse of dilute eruption columns, ballistic curtains can leave trailing fine ash that travel outwards as PDCs and collapsing vertically focused jets into a deep crater can result in expulsion-driven PDCs (Graettinger et al., 2014).

We use these new ideas as a framework to help interpret a well-exposed, upper Pleistocene phonolite volcano on the southern flanks of Tenerife, Canary Islands, Spain. The volcano, previously described as a tuff ring, is here redefined, in part, as a maar-diatreme volcano, the evidence for which we outline below. We detail and interpret the lithofacies of the pyroclastic deposits and the structure of the maar and then build an eruptive history, outlining the changes in eruptive drivers over time. The case study provides a useful model for how silicic maar-forming eruptions may proceed and the range and nature of hazards that they produce.

2. Geological background

Tenerife is a large, long-lived, ocean island volcano in the Canary Islands, Spain. Explosive volcanism, fed predominantly by phonolitic magmas. Started ~1.9 Ma and numerous Plinian deposits, along with phonolite and basalt lavas, constructed the Las Cañadas pyroclastic shield volcano which is capped by Las Cañadas caldera (Martí et al., 1994; Ancochea et al., 1999; Martí, 2019). Tephra fall deposits and ignimbrites from Las Cañadas volcano outcrop extensively along the southern coast of the island (Bryan et al., 1998; Brown et al., 2003; Brown and Branney, 2013; Pittari et al., 2006; Edgar et al., 2007, 2017; Davila-Harris et al., 2013; Davila-Harris et al., 2022). Concomitant with the explosive volcanism was persistent monogenetic basaltic volcanism focussed along the northwest, northeast and southern rift zones (e.g., Bryan et al., 1998; Carracedo et al., 2007). The caldera hosts the Teide-Pico Viejo-Montaña Blanca composite volcano, which has been the location for numerous basaltic and phonolite eruptions (Carracedo et al., 2003, 2007; García et al., 2011).

Caldera del Rey (CDR) is an eroded 0.95 Ma, phonolite monogenetic volcano in southwest Tenerife located 1 km from the coast (Fig. 1). It has been interpreted as a polygenetic tuff ring (Paradas Herrero and Fernandez Santín, 1984; Davila-Harris, 2011; Davila-Harris et al., 2022; Cas et al., 2022) and is one of two well preserved monogenetic phonolite volcanoes in the southern rift zone; the other is the Montaña Guaza lava dome and coulée (0.92 Ma Hernández-Pacheco et al., 1990). Phreatomagmatic volcanoes are rare on Tenerife and all occur close to the coast (De La Nuez et al., 1993; Clarke et al., 2009; Carmona et al., 2011).

3. Methods

Fieldwork centred around detailed logging of CDR deposits at 39 locations around the volcano, totalling 275 m of logged strata. A lithofacies approach, following that of Branney and Kokelaar (2002), was adopted for describing the deposits. Geological mapping was undertaken on Google Earth satellite images which were then georeferenced in ArcGIS Pro. Key features of the deposits were quantified in the field including height and wavelength of dune bedforms, and the size of ballistic blocks and their impacts sags, and their distance from the crater wall. We define proximal areas as those <1 km from the crater (on the volcano's flanks), and area beyond this as distal.

The pyroclastic deposits are indurated, and many pumice clasts are commonly partly altered to clay and zeolite minerals (e.g., Hernández et al., 1993), meaning that sieving and granulometric study of the deposits was not possible.

Pumice vesicularity was measured on 100 unaltered lapilli-sized clasts following the method of Houghton and Wilson (1989) taken representative beds for all Members except Member D, in which the pumice clasts were strongly altered or inaccessible. The lithic clast types were defined in the field and 500 lapilli-sized clasts were classified for representative lithic-rich beds in each Member. Maximum lithic clast size for the pumice fall deposits was determined following the methodology of Bonadonna et al. (2013). We follow the terminology of Brown et al. (2012) when describing ash aggregates: AP2 aggregates exhibit concentric structures (accretionary lapilli) and AP1 are internally massive (ash pellets).

Column heights for pumice fall deposits were estimated from limited crosswind isopleth data using the Biass et al. (2015) MATLAB implementation of Carey and Sparks' (1986) model, using a nominal lithic clast density of 2700 kg/m^3.

Nineteen pumice samples were analysed for major oxides and trace elements. Pumice samples were trimmed manually, and then cleaned in de-ionised water and an ultrasonic bath. Element concentrations were determined by x-ray fluorescence performed on a Philips PW 1400 X-Ray Fluorescence Spectrograph at 50 kV and 50 mA utilising PANalytical software at the Department of Geology, University of Leicester.

4. Results

4.1. Volcano morphology and physical characteristics

The CDR volcano was constructed at the foot of Roque del Conde: a steep, eroded remnant of a basaltic shield volcano that is partially buried by younger lavas and pyroclastic rocks. It consists of a large, keyhole-shaped crater, 2 km in length, formed from two overlapping craters: a larger north crater, 1000 m in diameter, and a smaller south crater, 675 m in diameter (Figs. 1 and 2a). The craters are elongated N 20° E and form an enclosed, flat-bottomed basin floored with pyroclastic and post-eruption sedimentary deposits that presently sits 100 m above sea level. The northern side of the north crater is enclosed by a 200 m-high ridge composed of basalt lavas of Roque del Conde (Morro Negro, Figs. 1 and 2a). The CDR deposits overlie a paleosol developed in a thin phonolitic ash layer, or overlie the rubbly tops of basaltic lavas.

A tephra ring rises ~90 m above the north crater and up to 40 m above the south crater (Fig. 1) and extends contiguously for 0.2–1 km south, east and west of the volcano. To the north and east, tephra ring deposits are plastered against steep slopes (Fig. 2a and b); on the south and west, CDR deposits were emplaced upon a paleoslope (5°–9°). The tephra ring has been mostly eroded from the steep slopes to the north and east. The tephra ring deposits are here divided into 6 lithologically distinct and mappable lithostratigraphic members (A-F; Fig. 3).

Isolated outcrops of CDR deposits occur at distances of several kilometres: 2.5 km northwest at the northern end of Fañabe beach, 1.8 km west on the east side of Barranco de Bisechi at 430 m above sea level (Fig. 1); and 3.7 km southeast on the north of the autopista at Barranco

Fig. 2. The Caldera del Rey volcano. A) Satellite image showing north and south crater and relationships between tephra ring (pale deposits) and topography. Present crest of tephra ring roughly indicated by perimeter road. B) Tephra ring composed of Member D deposits mantling steep slope of Morro Negro. Location shown in A (28° 5′8.29"N 16°43′2.81"W). C) Old road cut through the south crater wall, showing deposits erupted from north crater (Members C-E) draping crater wall cut through Member B. Location shown in A (28° 4′20.46"N 16°43′9.50"W) [COLOUR].

de los Chijafes. The entire western flank of the tephra ring has been extensively urbanised, and outcrops become sparse amongst the buildings. The floor of the crater is presently covered in a banana plantation.

Juvenile clasts, including pumice and ash, are commonly altered, sometimes strongly, and the glass has been partially replaced by clay and zeolite minerals. This is particularly marked on the exteriors of pumice clasts. At many outcrops the deposits, including clast-supported pumice lapilli deposits are lithified via this alteration process.

4.2. Pyroclastic deposits

4.2.1. Member A

Member A is a coarse-grained, clast-supported, pumice lapilli deposit with a maximum preserved thickness of ~11 m (Fig. 4a). It outcrops in a narrow strip of heavily urbanised land between the volcano and the coast on the south and southwest flanks of the volcano and is well exposed next to the Playa de Las Americas bus station. At the north end of Fañabe beach, its most distal, off-axis outcrop, Member A is 1.2 m thick. Limited isopach data constrain the dispersal of the umbrella cloud to the west of the south crater (Fig. 5).

The pumice clasts are angular to sub-angular and typically make up 60–90 vol% of the deposit. They range in size from coarse ash to block size. Qualitatively, the sorting appears in increase with distance from the vent, with proximal deposits showing abundant coarse pumice and lithic blocks. Lithic clasts account for 10–40 vol% of the deposit (Fig. 5). The lithic population is dominated by aphanitic and porphyritic basalt lava (60%), alongside ankaramite lava (16%), and oxidised scoria, amygdaloidal basalt lava, and pyroclastic rocks (5–9% each). Obsidian clasts account for <1%. Lithic blocks (lB) reach 1.4 m in diameter in some proximal outcrops and some sit in impact sags.

Member A is divided into three sub-units (Figs. 4a and 5). Unit 1 is a < 6 m-thick, massive coarse-grained pumice lapilli deposit (lithofacies mL, Table 1) with a 4 cm thick fine lapilli basal layer. It contains ~15–20 vol% lithic clasts. Unit 2 is a 3 m-thick massive lapilli deposits with lithic blocks (Fig. 4a). Unit 3 is >1.5 m thick, and is characterised by clast-supported, lapilli beds, each 2–10 cm thick (lithofacies bL, Table 1) with variable lithic clast contents.

4.2.2. Member B

Member B is >5.5 m thick in proximal areas and is composed of

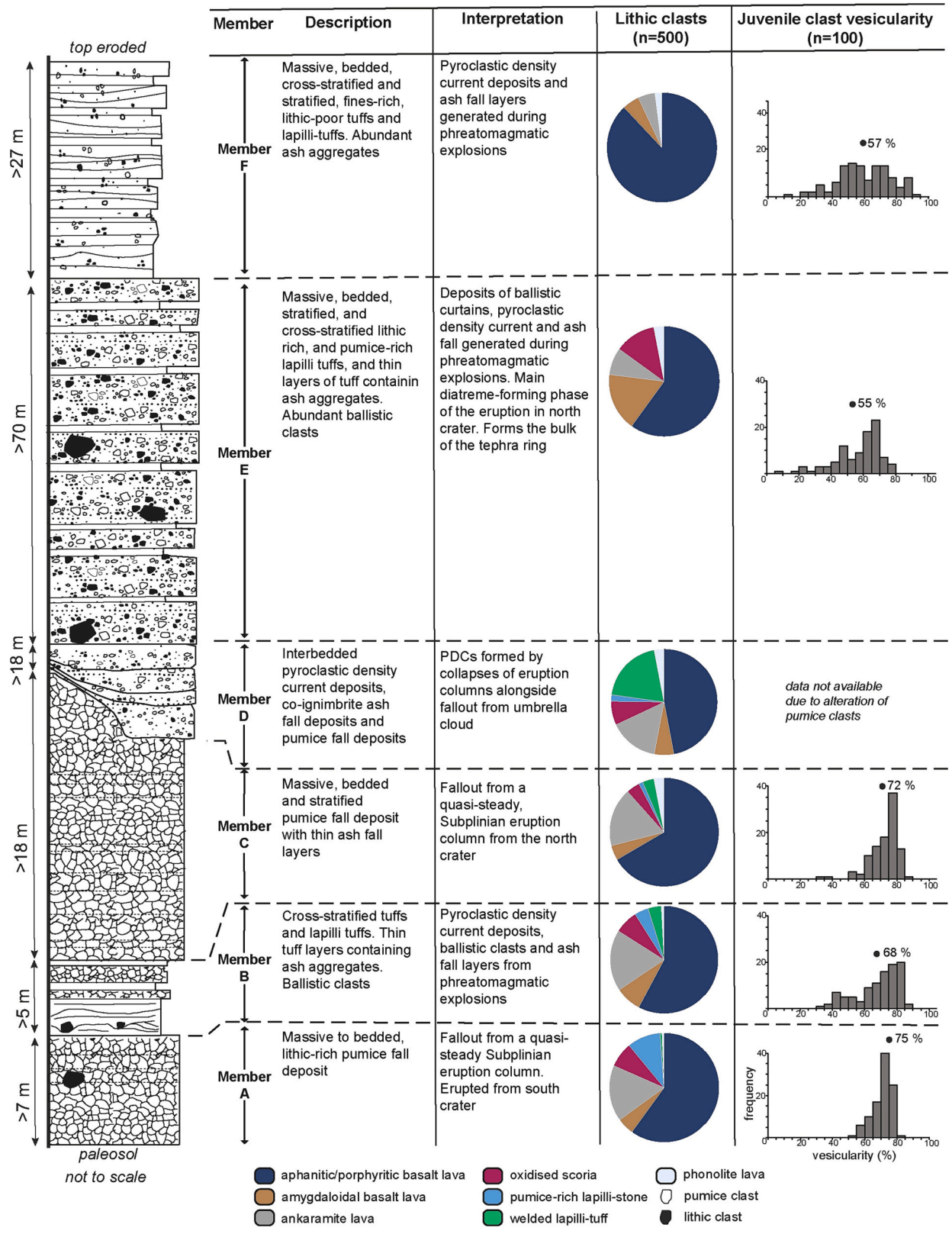

Fig. 3. Summary general vertical section through pyroclastic deposits of the CDR tephra ring [COLOUR].

massive, bedded and cross stratified tuff deposits (mLT, bLT, xsT, Table 1), layers of clast-supported pumice lapilli (bL), tuff layers with accretionary lapilli (mTacc) and layers of massive tuff breccia (mTBr) and lithic blocks (lB) (Fig. 4a, b, c and e). In distal areas, it is composed of layers of pumice lapilli (bL) and layers of tuff (mTacc; Fig. 6). It is 1.4 m thick at its most distal preserved outcrop, (Fañabe beach, Fig. 1). The contact between Member A and Member B is sharp in distal areas, but gradational over 50 cm in proximal areas where the base of Member B is taken as the first appearance of fine-grained, whitish tuff beds. The lithic population is similar to that of Member A (Fig. 3).

Fig. 4. Caldera del Rey Members A-C. A) Proximal Member A pumice fall deposit, overlying thin reworked volcaniclastic sediments and thick paleosol developed in rubbly top of lava (Los Cristianos bus station, 28° 4′16.89”N 16°43′39.15”W). B) Ballistic clast in impact sag in Member B in TF-1 autopista road cut (28° 4′50.29”N 16°43′45.19”W; no longer exposed). C) Member B showing large dune bedform and lithic clast-rich layers. Metre rule for scale (Calle Belgica, 28° 4′30.18”N 16°43′30.96”W). D) Roadcut through Member C. Subvertical grooves are manmade (Calle Belgica, 28° 4′28.32”N 16°43′30.15”W). E) Outcrop of Members A-D next to TF-1 autopista (28° 4′53.53”N 16°43′44.29”W). Note how Member D pyroclastic density current deposits (right) thin and pinch out over paleo-topography (towards left) [COLOUR].

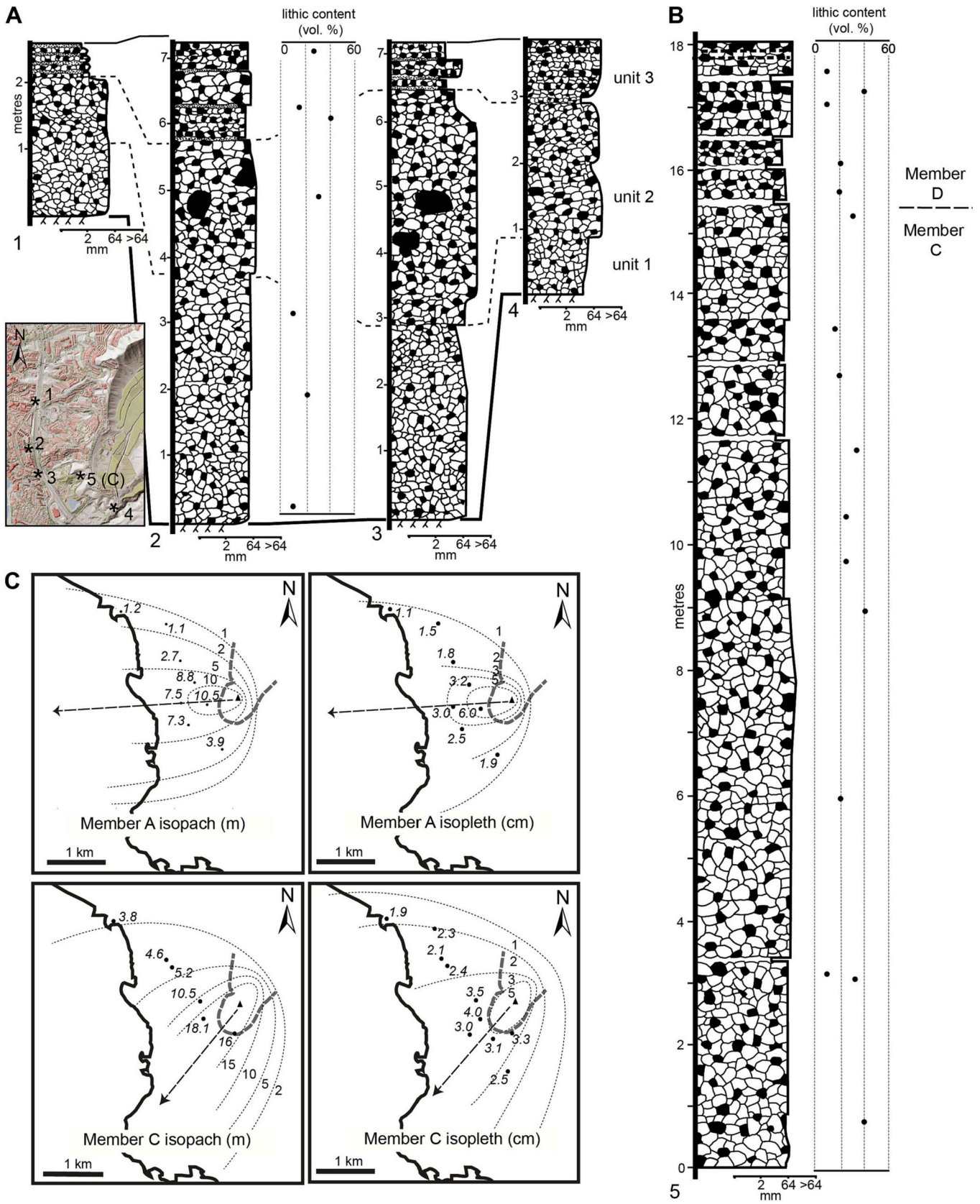

Fig. 5. Pumice fall deposits of the CDR eruption. A) Measured sections through Member A. B) Proximal measured section through Members C and D. Contact between Members is not clear. C) Partial isopach and isopleth maps for Members A and C pumice fall deposits. Numbers in italics are average maximum lithic lapilli dimensions [COLOUR].

Table 1
Summary characteristics of lithofacies of the CDR deposits.

Lithofacies	Description	Interpretation
Massive to crudely bedded tuff breccia (mTBr, dbTBr)	Chaotic, poorly sorted, clast- to matrix-supported pumice and lithic lapilli and blocks in a tuff matrix; massive or crudely bedded; bedding often not traceable over more than a few metres; forms units up to 2 m thick that are laterally continuous.	Near optimal scaled-depth explosions; emplacement by ballistic curtains (e.g., Valentine et al., 2015)
Massive lapilli tuff (mLT); lithic-rich massive lapilli tuff (lmLT)	Variable proportions of lithic and pumice lapilli, matrix-supported in poorly sorted, fine to coarse-grained tuff matrix; occurs in m-thick, laterally continuous or lenticular units.	Deposited from fluid escape-dominated depositional flow-boundary of PDC; or near optimal scaled-depth explosions and emplacement by ballistic curtains (e.g., Valentine et al., 2015);
Diffuse bedded lapilli tuff (dbLT); lithic-rich diffuse bedded lapilli tuff (ldbLT);	Composition as mLT/lmLT; discontinuous, sub-parallel and undulating diffuse bedding defined by cm-thick lithic horizons or by thin (<2 cm) lapilli-poor layers; individual beds persistent over 2–6 m.	deposited from fluid escape-dominated depositional flow-boundary of PDC; diffuse bedding results from unsteadiness.
Stratified lapilli tuff (sLT); Stratified tuff (sT)	Alternating moderately sorted fine-grained layers and more poorly-sorted coarser-grained layers; matrix supported sub-angular to sub-rounded pumice and lithic lapilli; parallel to sub-parallel strata <1–5 cm thick in sets 4–60 cm; very low-angle truncations are present; laterally persistent over 10s–100s m	Deposition from traction-dominated flow-boundaries of fully dilute PDCs; deeper-than-optimal scaled depth explosion, emplacement by expulsion-driven PDCs (e.g., Valentine et al., 2015)
Pumice lenses (pLens)	Clast-supported, rounded pumice lapilli and blocks in a tuff matrix; forms lenses <1 m high by <2 m wide	Marginal or terminal pumice levees formed by granular segregation of pumice clasts within PDCs (e.g., Branney and Kokelaar, 2002)
Cross-stratified lapilli tuff (xsLT); Cross-stratified tuff (xsT)	As stratified lapilli tuff (sLT); low-angle cross-stratification defined by mm-cm thick strata; foreset laminae dip ~5–20°; bedform amplitudes 10–100 cm; occurs in cm-dm thick packages	Deposition from traction-dominated flow-boundaries of fully dilute PDCs; deeper-than-optimal scaled depth explosions, emplacement by expulsion-driven PDCs (e.g., Valentine et al., 2015)
Massive tuff (mT)	Fine-grained tuff wth minor pumice and lithic lapilli (<5%) in beds 1–20 cm thick; massive to diffusely stratified; mantles topography	Deposition from ash-rich PDCs or ash fall from eruption column-fed or co-ignimbrite ash clouds
Massive accretionary lapilli-bearing tuff (mTacc)	As massive tuff (mT); contains matrix to clast-supported, whole and broken AP2 ash aggregates (accretionary lapilli) 3–15 mm diameter; generally massive or weakly bedded; occurs as individual beds or in stacked sets several metres thick in scale	Deposited from moisture-rich PDCs; ash aggregates grew in eruption column, ash clouds or co-ignimbrite clouds and fell into current
Massive ash pellet-bearing tuff (mTpel)	Massive clast-supported AP1 ash aggregates (ash pellets) in an ash matrix; may show normal grading; beds laterally persistent up to several km	Ash fall deposits from moisture-rich eruption column-fed ash clouds or co-ignimbrite ash clouds
Bedded tuff (bT)	Tuff with rare pumice and lithic lapilli and matrix-supported to clast-supported ash aggregates; mm- to cm-scale parallel laminations; laterally persistent beds 1–5 cm thick that drape topography	Ash fall deposits from eruption column-fed or co-ignimbrite ash clouds
Lithic blocks (lB)	Angular lithic blocks, up to 2 m in diameter; some sat in impact sags	Ballistic clasts ejected during phreatomagmatic and magmatic explosions
Massive lapilli (mL)	Massive, clast-supported angular pumice lapilli and rare blocks, and lithic lapilli (2–40 vol%); occurs in beds up to several metres thick	Fallout of pumice and lithic lapilli from eruption columns and umbrella clouds under steady conditions
Bedded lapilli (bL)	As mL but with cm-scale bedding defined by variations in grainsize and proportions of lithc and pumice components	Fallout of pumice and lithic lapilli from eruption columns and umbrella clouds under unsteady conditions

Grainsize: Br, Breccia; T, tuff; LT, lapilli tuff; L, lapilli; *Composition*: l, lithic-rich; acc, accretionary lapilli-bearing; pel, ash pellet-bearing; *Structure:* m, massive; db, diffuse-bedded; b, bedded; s, stratified; xs, cross-stratified;. Naming scheme follows that devised by Branney and Kokelaar (2002). Lithic-rich lithofacies contain >30 vol% lithic lapilli.

Member B is here divided into four units. In proximal regions, unit 1 is a 2-m-thick sequence of thin bedded and massive tuffs (see Table 1) containing matrix-supported accretionary lapilli and coated pellets (mTacc, mTpel) alternating with massive lithic-rich tuff breccias. Impact sags are common along the bases of the tuff breccias (Fig. 4b and c). Upper parts are cross-stratified and exhibit dune bedforms with amplitudes of 50–80 cm. In distal parts, unit 1 consists of 1 m of parallel-bedded and stratified tuff with accretionary lapilli (bTacc; Figs. 4e and 6). Unit 2 has a maximum observed thickness of 1.2 m thick and is composed of thin to medium bedded pumice lapilli (bL) and bedded tuffs (bT) and contains scattered ballistic blocks sat in impact sags. In distal regions, it is thinner, finer-grained and lacks ballistic clasts. Unit 3 comprises several decimetres of parallel-bedded tuff with scattered accretionary lapilli and is a useful marker horizon traceable across the western flanks of the volcano (Figs. 4c and d, 6). Unit 4 consists of up to 1.2 m of bedded pumice lapilli deposits and tuff layers (bL, bT). Unit 4 passes gradationally up into Member C and the contact is difficult to define (Fig. 4e).

4.2.3. Member C

Member C is a sequence of coarse-grained, moderate to poorly sorted, massive to bedded pumice lapilli (mL, bL) deposits and minor thin tuff beds (bT), with a maximum observed thickness of ~15 m (Figs. 4d and e and 5). It outcrops on the southern and western flanks of CDR (Fig. 1) and is well exposed in roadcuts behind the Siam Park waterpark (Fig. 4D). In proximal locations, pumice clasts average 1–3 cm in diameter, but some reach 35 cm in diameter. Centimetre to decimetre-scale bedding becomes more pronounced and thinner with distance from the vent and is defined by slight variations in grainsize and by variations in lithic clast content (from 15 to 40 vol%). The lithic population is similar to the preceding two members.

Member C has a dispersal axis of S 35° W and isopleth data indicate a

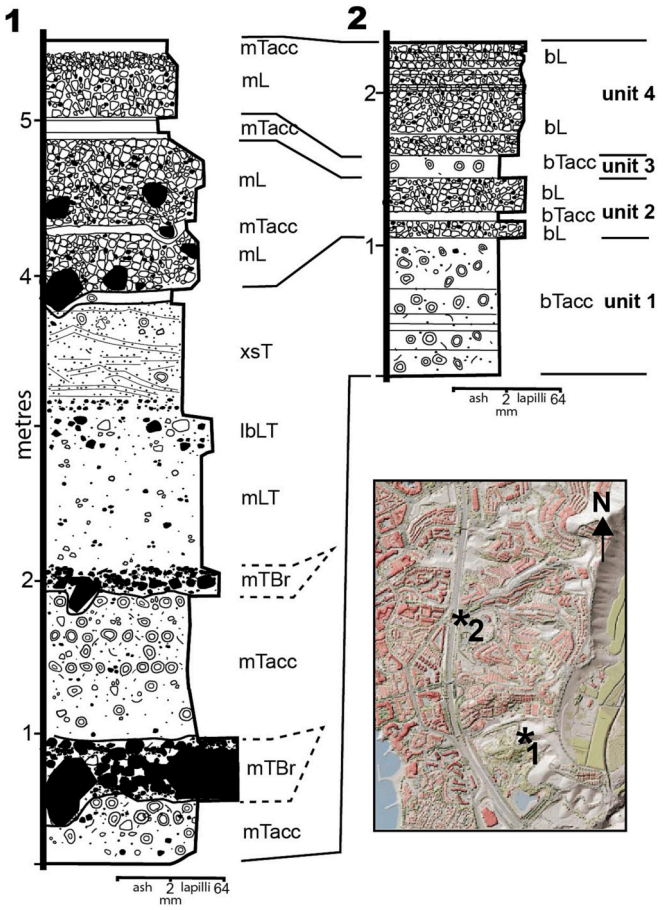

Fig. 6. Measured sections through Member B. Lithofacies codes defined in Table 1 [COLOUR].

column height of 11.5 km (Fig. 5). At most locations it conformably overlies Member B, but in the southern margin of the south crater it drapes an unconformity that cuts through Member B (Fig. 2c). Member C passes up into bedded pumice and tuff deposits of Member D (Fig. 4e).

4.2.4. Member D

Member D conformably overlies Member C and is well-exposed on the west flank of the volcano in roadcuts along the autopista TF-1 at Torviscas (Fig. 1) and outcrops over an area of >2 km^2. It comprises >18 m of lenticular beds of bedded, massive and stratified lapilli tuff (mLT, sLT, bLT, lmLT, Table 1), pumice-rich lenses (pLens) that are interbedded with, and pass laterally into, parallel-bedded tuff beds (mT, bT) and pumice lapilli beds (pL) (Fig. 7). Tuff beds drape the marginal margins of the lapilli-tuff beds and pumice lenses (Fig. 7d).

The lapilli-tuffs fill a paleovalley north of a ridge draped by lower members (Fig. 7e), that probably represents the extension of the NE-SW oriented Morro Negro ridge towards the coast under the CDR deposits (Fig. 1). They pinch-out upslope (west) towards the crater and pinch-out southeast against the ridge. The units have tabular to wedge-shaped geometries and locally erosive contacts. Lower beds pinch out laterally against the buried Morro Negro ridge. Some exhibit marginal pumice lenses (pLens, Table 1), and some are draped by, and pass into, thin tuff beds (Figs. 4e and 7), some of which contain ash aggregates. Upper beds of lapilli-tuff exhibit tabular geometries as a result of the filling of the paleovalley.

On the SW side of CDR, Member D comprises ~4 m of centimetre-thick, parallel-bedded tuff beds, some of which contain ash aggregates, and decimetre-thick pumice lapilli beds: the lapilli-tuff beds are absent (Fig. 5). Member D here is conformable with the pumice lapilli beds of Member C. The contacts with the enclosing members are difficult to define. The lower contact of Member D is taken as the first laterally continuous tuff bed, and the upper contact is defined by the appearance of chaotic, clast-rich, massive tuff breccias, and abundant impact sags characteristic of Member E.

The lithic population of Member D differs from Member A-C by lower abundances of aphyric and porphyritic lavas (47%), and increased abundances of dense, glassy welded lapilli-tuff (20%, Fig. 3).

At Fañabe beach (Figs. 1 and 12c), the member consists of 80 cm of thin to medium thickness, parallel bedded, accretionary lapilli-bearing tuffs and pumice lapilli beds, overlain by <1 m of stratified tuffs, cross-stratified tuffs and bedded lapilli (see Table 1).

4.2.5. Member E

Member E consists of alternating beds of massive, bedded tuff breccia and lapilli tuff (mTBr, mLT, dbTBr, dbLT), cross-stratified tuff and lapilli-tuff (xsT, xsLT), tuff beds (mT, bT), accretionary lapilli-bearing tuff (mTacc), and abundant lithic blocks (lB) up to 2.5 m in diameter (Supplementary information 1, and Fig. 8a). At most proximal locations, Member E is tens of metres thick, and may exceed 70 m thick on the eastern side of the north crater (Fig. 8). It is radially dispersed around CDR (Fig. 1) and forms the greatest thickness of the tephra ring. Beds dip at shallow angles (<8°) away from the vent on the western flank but are steeper where draping pre-existing topography to the north and east (Figs. 1 and 2b). The deposits locally thicken into topographic lows. In southern areas the lower contact with Member C is gradational over 0.3 m, but in western areas the contact is sharp.

In proximal areas Member E is composed of a sequence of alternating coarser-grained and finer-grained beds that form depositional couplets (Fig. 8). A typical couplet is composed of a 1–3 m thick bed of massive tuff breccia overlain by a thin bed of massive accretionary lapilli-bearing tuff, stratified tuff or lapilli tuff. The bases of the couplets, and the capping beds of the underlying couplets are commonly strongly disrupted by impact sags, some of which contain lithic blocks (Fig. 8c). Individual beds of massive tuff breccia trace laterally over tens to hundreds of metres where outcrops allow, and generally fine and thin with distance. Several thin tuff beds correlate widely across the southern flank of the volcano. The lithic population diverges from the previous members and lacks welded lapilli-tuff and lapilli stone clasts (Fig. 3).

At distances of ~1 km from the vent), Member E is lithologically similar to proximal regions, but the couplets are thinner and there are numerous beds of cross-stratified lapilli-tuff. Dune bedforms occur on a range of scales, but typically have wavelengths of <2 m and amplitudes of <0.3 m (see supplementary information file 1). Cross-stratification is generally low angle (5°–15°), and individual strata pinch and swell over distances of metres (Fig. 8d). The dimensions of the dune bedforms overlap bedforms measured at other similar volcanoes (see supplementary information file 1).

4.2.6. Member F

Member F is >27 m-thick succession of bedded, cross-stratified and stratified tuffs (bT, xsT, sT, Table 1), ash aggregate-bearing massive and bedded tuffs and lapilli tuffs (mTacc, mTpel) and massive lapilli tuff (mLT; Fig. 9) and it fills the southern crater (Fig. 1). It outcrops only along a man-made gully cut through the crater rim where it and Member C is draped over a crater wall cut through Member B (Fig. 2c). The original extent of Member F is not known.

Beds in Member F exhibit scour surfaces and pinch-and-swell and lenticular geometries. Many beds thin against the slope of the inner crater wall or pinch out against it (Fig. 10b). Some beds have partly slumped back into the crater.

Member F is generally fine-grained and lapilli-poor. The lithic clast population sampled from a massive lapilli tuff bed, is the least diverse population in the CDR, and consists mostly of various basaltic lava lithologies and a small percentage of phonolite lava clasts. Pyroclastic lithic clasts are absent.

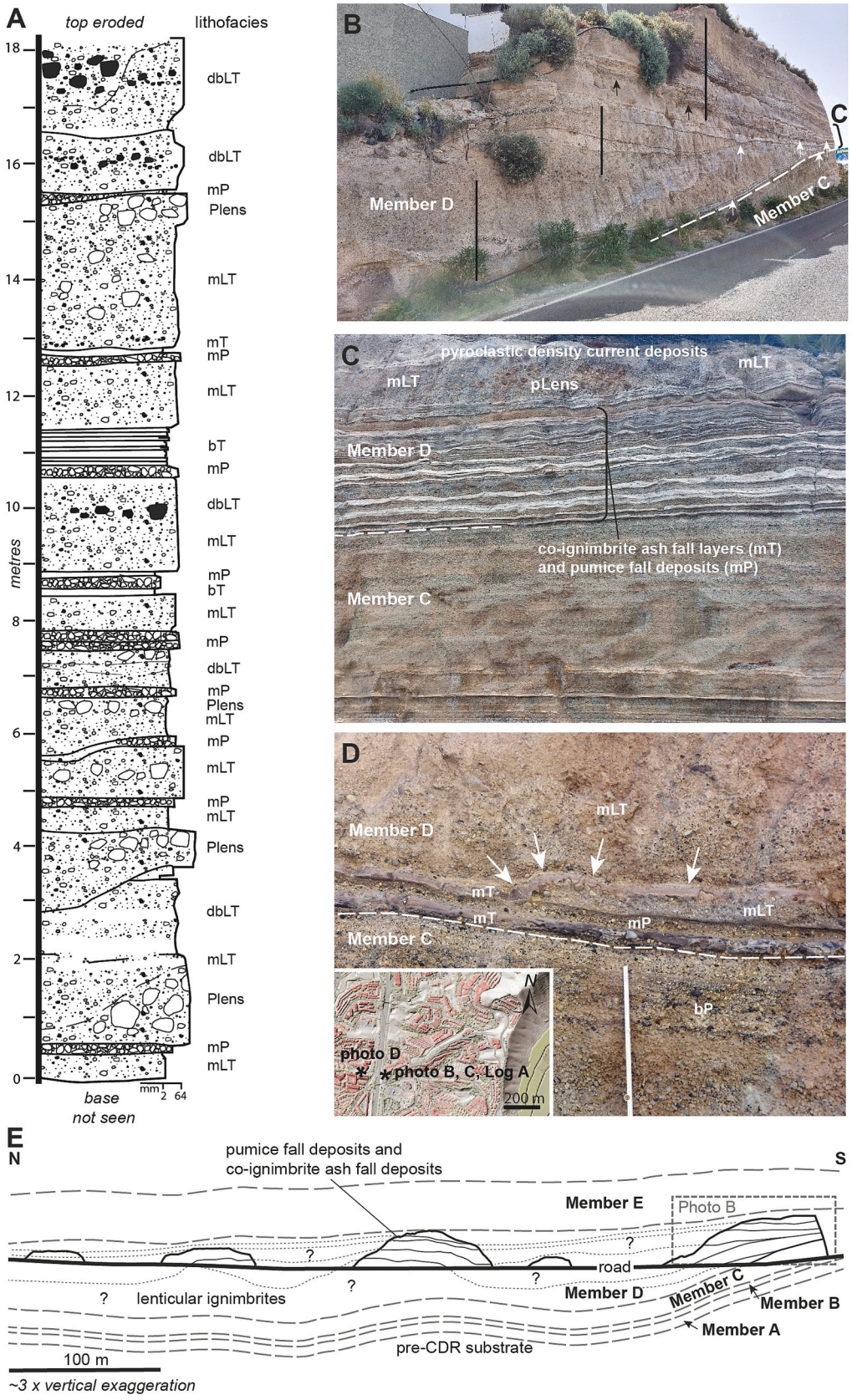

(caption on next page)

Fig. 7. Member D. A) Composite log through paleovalley-filling pyroclastic deposits of Member D. Section comprises a succession of pyroclastic density current deposits, alternating with pumice and co-ignimbrite ash fall deposits (road: TF-481, 28° 4′53.53”N 16°43′44.29”W) B) Section logged in A (black lines indicate vertical sections). Pyroclastic density current deposits thin and pinch out against paleoslope. White arrows indicate terminations of PDC deposits. Black arrows indicate pumice fall deposit interbedded with PDC deposits. Same location as A. C) Paleo-ridge preserving mostly pumice fall and co-ignimbrite ash fall deposits that correlate with those in A. Same location as A. D) Road section orthogonal to those in A and B, showing draping of the upslope termination of PDC deposit by an ash layer (top marked by arrows) inferred to be a co-ignimbrite ash layer (Calle Antonio Navarro, 28° 4′54.50”N 16°43′49.02”W) E) Schematic road section along TF-481 showing reconstructed cross-section through Member D deposits in context of overlying and underlying members. The paleotopography on the south end of the road cut probably represents the buried Morro Negro ridge [COLOUR].

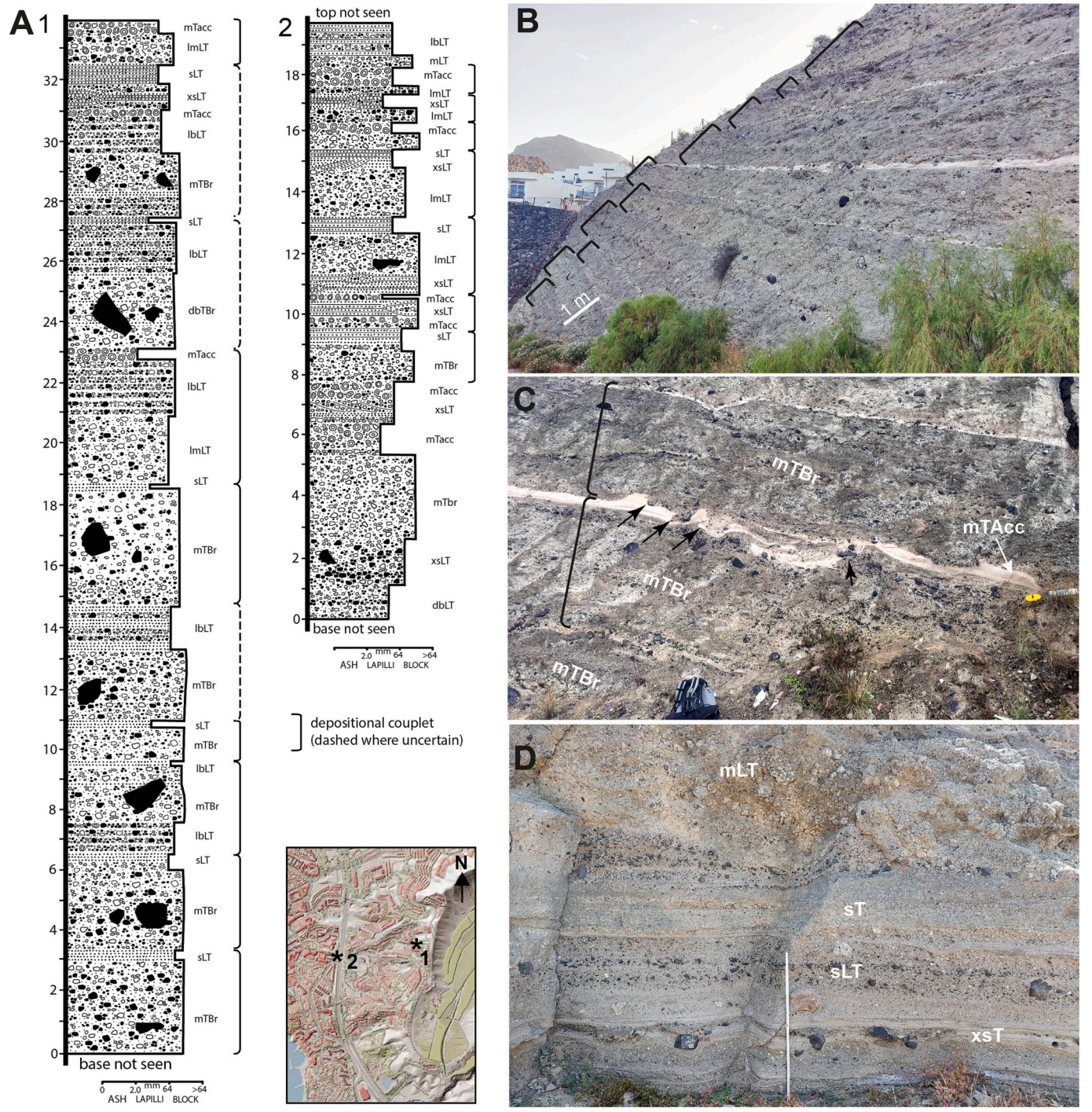

Fig. 8. Member E. A) Measured sections through Member E. Inset map shows location of logs. B) Depositional couplets consisting of thick beds of massive tuff breccia (mTBr) capped by thin pale-coloured tuff beds (bT, bTacc). (Avenida Francia, 28°05′04.42”N 16°43′13.50”W). Rucksack for scale. C) Depositional couples showing detail of thin tuff beds disrupted with ballistic blocks and impact sags (Calle Madrid, 28°05′04.18”N 16°43′18.25”W). D) Cross-stratified lapilli-tuff deposits. Same location as C. Lithofacies codes defined in Table 1. 30 cm rule for scale [COLOUR].

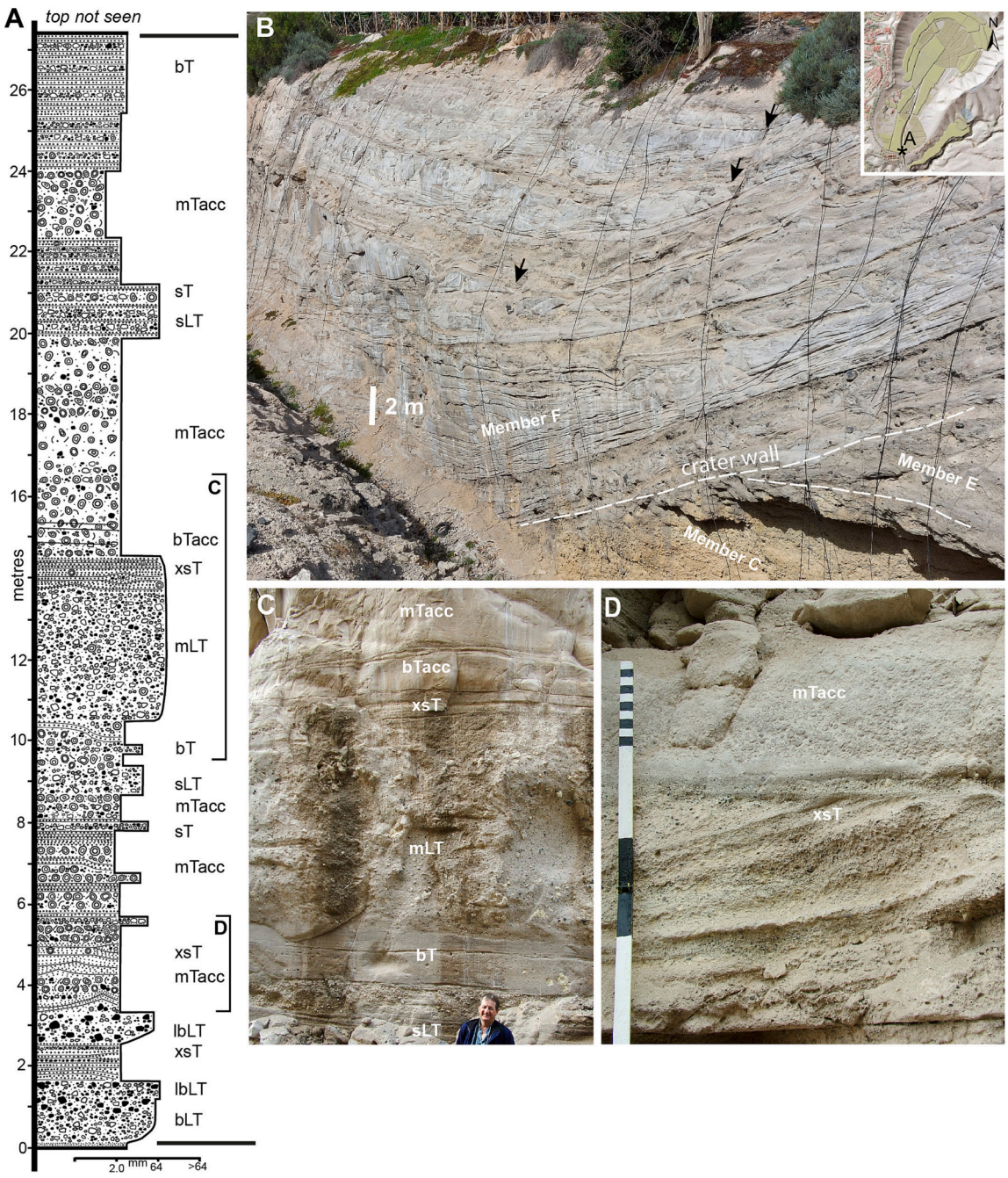

Fig. 9. Member F deposits (28° 4′20.46”N 16°43′9.50”W). A) Measured section through Member E deposits in the southern edge of south crater. B) Member F deposits banking up against the inner crater wall. Arrows indicate beds that thin against the topography. C) Massive lapilli-tuff bed. Position marked in log. D) Cross-stratified tuff overlain by massive accretionary lapilli bearing tuff. Current from right to left. Smallest divisions on scale are 1 cm. Lithofacies codes defined in Table 1 [COLOUR].

A variety of ash aggregates are present in Member F. The most frequently occurring type are weakly structured aggregates (AP2 aggregates of Brown et al., 2012) comprising a massive, coarser-grained ash core that resembles the matrix of the beds they occur within, surrounded by a ~ 0.5 mm thick, finer-grained rim. They are generally subspherical, average 4 mm in diameter, and occur matrix-to clast-supported (20–40 vol%) in tuff beds. AP2 Aggregates with well-developed concentric structures (accretionary lapilli) and multiple fine-grained rims that become finer-grained outwards, are less abundant (10–20 vol%) and typically occur matrix-supported, but clast-supported beds are present. Ash pellets (AP1 aggregates) lack the finer-grained outer rim of weakly structured aggregates. They are typically clast-supported and cap tuff beds that contain AP1 aggregates. A typical sequence in Member F consists of a 10–20 cm thick tuff bed in which aggregate concentrations increase upwards and become dominated by weakly structured aggregates or ash pellets.

4.2.7. Distal outcrops

Distal deposits of the CDR eruption outcrop at Fañabe beach, Risco Bisechi (Fig. 1) and Barranco de los Chiafos (4 km from CDR, 28° 3′30.21”N, 16°41′11.07”W). Those to the east and southeast are composed predominantly of parallel-bedded tephra fall deposits and correlations with proximal deposits are uncertain. Approximately 4 m of tephra fall deposits are preserved at Barranco Risco Bisechi, located 1.7

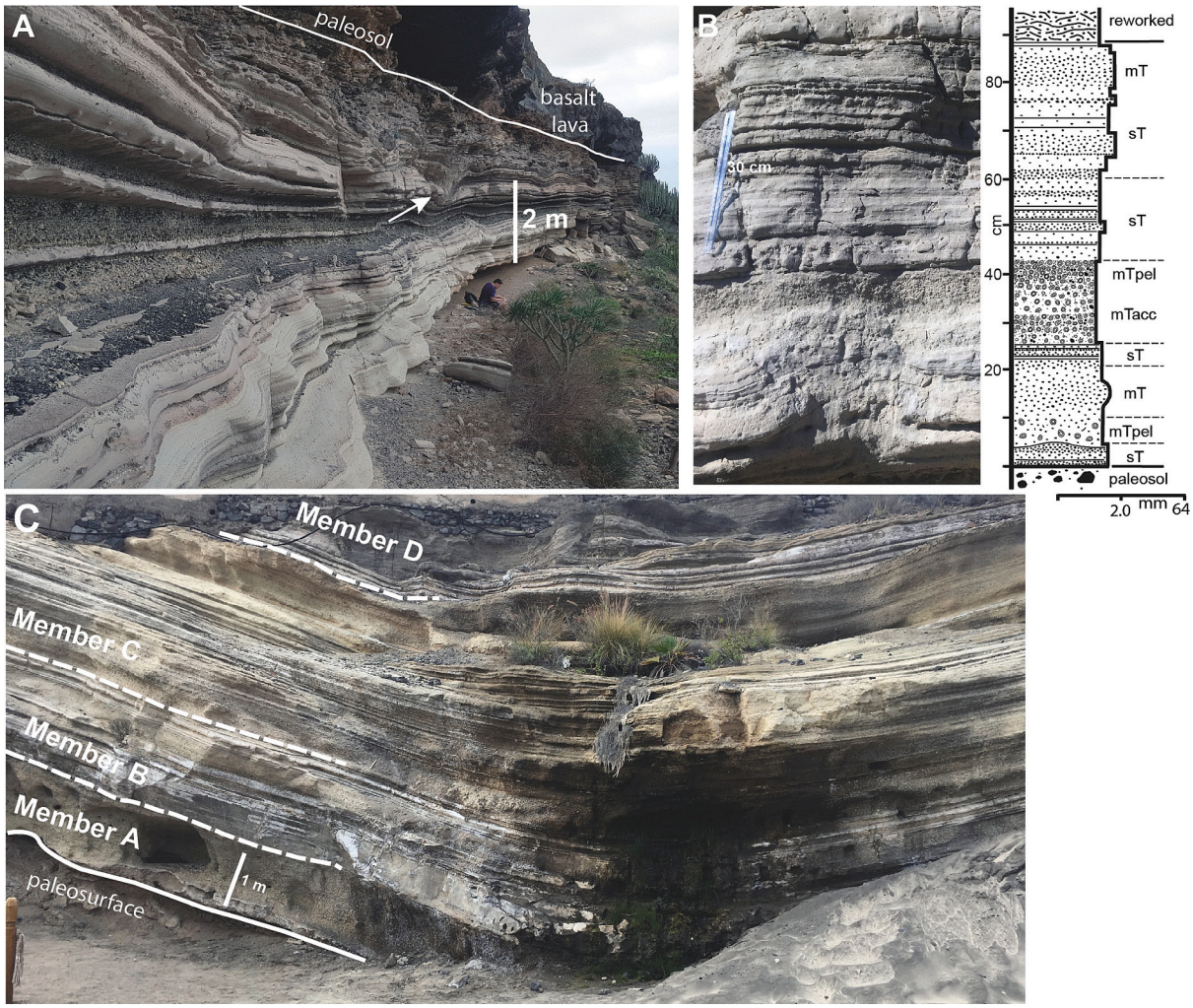

Fig. 10. Distal outcrops of the CDR deposits. A) ~4 m-thick sequence of ash fall and fine pumice lapilli fall deposits, 1.5 km east of north crater at Barranco Risco Bisechi. Correlations with proximal deposits uncertain (28° 5′6.69"N 16°41′53.96"W). Arrow points to impact sags. Outcrops sits 300 m above crater floor. B) Log and photo of distal deposits north of Montaña Guaza at Barranco de los Chiafos, 4 km SE of CDR (28° 3′30.84"N 16°41′12.18"W). Correlations with proximal deposits uncertain. Lithofacies codes defined in Table 1. C) Distal deposits at Fañabe beach (28° 5′19.96"N 16°44′23.31"W) [COLOUR].

km east of the volcano, at an altitude of 400 m (~300 m above the present crater floor, Figs. 1 and 10a). The deposits here consist of centimetre-thick white tuff beds that commonly contain coated pellets and that are interbedded with thin, lithic-rich, pumice fall deposits. Ballistic clasts up to 50 cm in diameter, of lavas and pumice, and impact sags, are present along some horizons (Fig. 10a). At Barranco de los Chiafos, CDR deposits are composed of 90 cm of parallel bedded and stratified white tuffs (Fig. 10b). Some beds contain coated pellets and one 17 cm thick tuff bed grades upwards from matrix-supported accretionary lapilli into clast-supported coated pellets, similar to some beds in Member E. We infer that the bulk of these distal deposits correlate with parts of Members B, D and E, because Members A and C were dispersed to the west/southwest. Distal deposits at Fañabe beach consist of several metres of parallel-bedded pumice and ash layers belonging to Members A, B, C and D, although correlations are uncertain due to the distance from proximal outcrops.

4.3. Texture, geochemistry and petrography of juvenile material

The juvenile pumice is pale green-grey, sparsely porphyritic to aphyric. Phenocryst phases include sparse sanidine up to 10 mm in length, black amphibole up to 5 mm length and small biotite microphenocrysts. The groundmass contains glass and altered sanidine microlites. Vesicular pumices are characterised by vesicles ranging in size from microns up to >1 cm (Fig. 11). Most pumice clasts have prismatic in shape and some large pumice blocks exhibit crude columnar-jointed exteriors. Some dense, incipiently to poorly vesicular clasts exhibit vague flow banding (Fig. 11).

Juvenile clasts exhibit vesicularity indices from 20 to 85 vol% (incipiently vesicular to extremely vesicular, following Houghton and Wilson, 1989) (Supplementary information 2, Fig. 3). There are marked differences in both the vesicularity indices (mean vesicularity) and in the vesicularity range of juvenile material in Members A-F. Juvenile clasts in Members A and C have vesicularity indices of 72 vol% and 75 vol% (highly vesicular), respectively, narrow ranges of values and a broadly unimodal distribution of vesicularity values. Conversely, juvenile clasts extracted from Members B, E and F have lower vesicularity indices (moderately vesicular, 68 vol%, 55 vol% and 57 vol%, respectively) and a greater range of values (Fig. 3). Member E exhibits a bimodal frequency distribution with peaks at 70 vol% and 50 vol% vesicularity. Members, B, E and F contain minor modes of poorly vesicular juvenile material (20–40 vol% vesicularity). Minor quantities of obsidian lapilli in Member A are considered juvenile.

The Caldera del Rey juvenile material is variably vesicular phonolite pumice (55–61 wt% SiO_2, 12–14 wt% $NA_2O + K_2O$, for data see Supplementary information 2). Its composition sits within the range of other

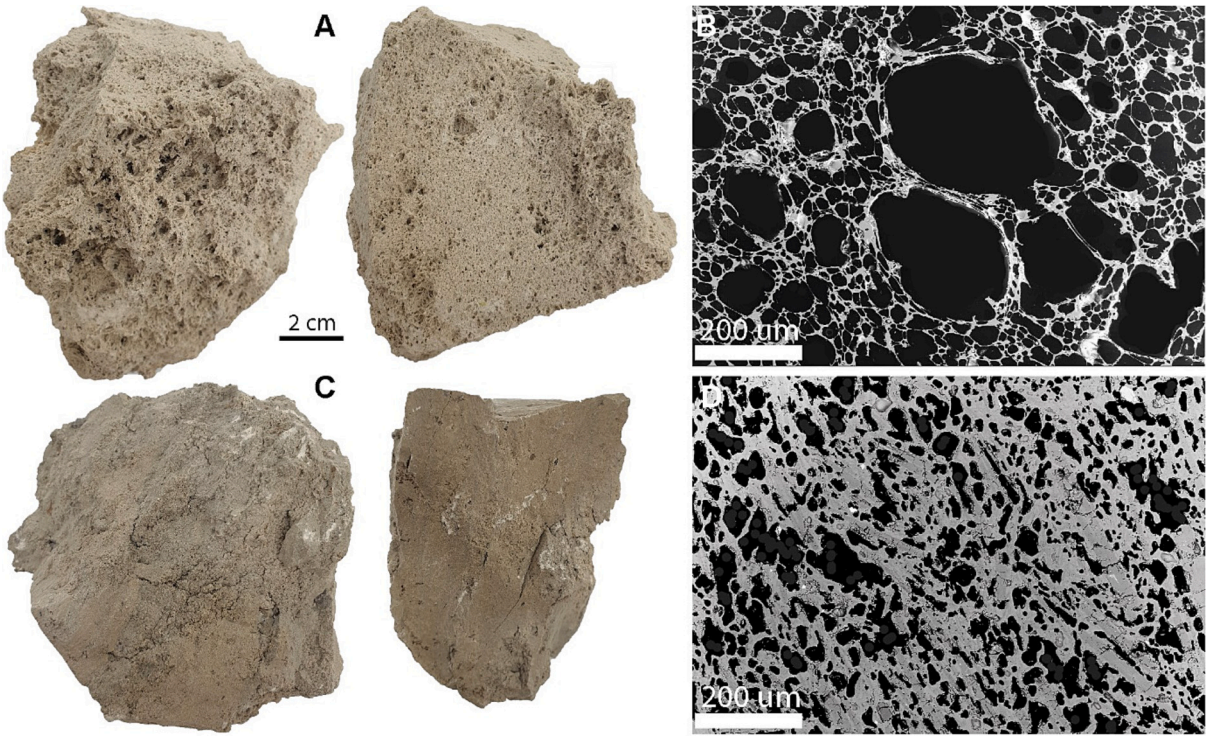

Fig. 11. Juvenile material end-members. A) Vesicular pumice from Member A with micro- and macro-vesicles. B) BSE image of pumice clast with a vesicularity index of 82%. C) dense juvenile clasts from Member F. Clast on right exhibits weak flow banding. D) BSE image of pumice clast from Member F with vesicularity index of 35% [COLOUR].

phonolite lavas and pyroclastic deposits on Tenerife (Fig. 12). There is no systematic trend in composition with time through the deposit.

5. Interpretation and discussion

5.1. Pyroclastic deposits

Member A represents the opening phases of the CDR eruption and its sheet-like, coarse-grained, framework-supported nature and angular pumice clasts indicates it is a pumice fall deposit dispersed west of the volcano (Fig. 13a). Limited isopach data suggest a vent within the south crater (Fig. 5). Changes in grainsize (Fig. 5) record changes in column height. The high lithic clast contents (>10–40 vol%) reflect erosion of a conduit excavated through basaltic lavas and pyroclastic deposits (ignimbrites, scoria deposits) (Fig. 1). Lithic blocks, some of which sit in impact sags, are interpreted as ballistic clasts, or as clasts released from the margins of the eruption column. Centimetre-scale bedding in unit 3 records the onset of marked unsteadiness in the plume. Crosswind isopleth data indicate column heights of ~8 km consistent with Subplinian activity (computed using Carey and Sparks, 1986; reported in (supplementary information file 2).

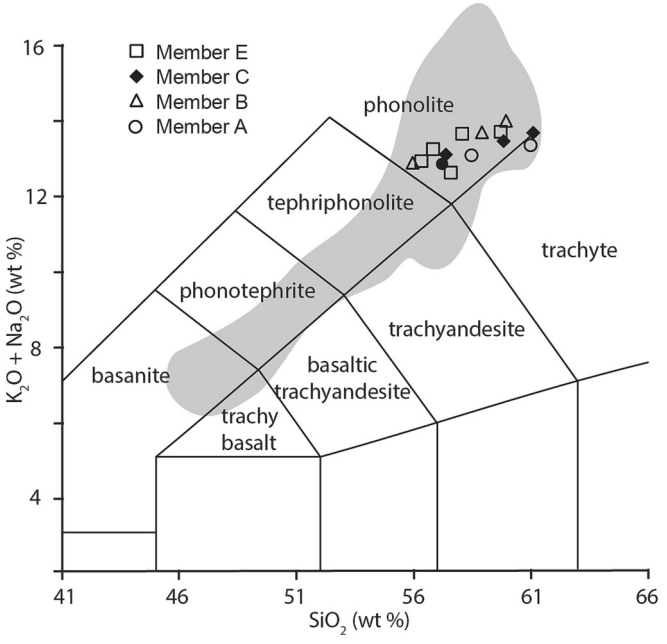

Fig. 12. Total alkali-silica plot for CDR juvenile material. Shaded field is Teide-Pico Viejo rocks (Ablay et al., 1998).

Member B, thickest around the south crater, records an abrupt change in eruption dynamics. The ash-rich beds, low-angle dune bedforms, abundant ash aggregates and clast-supported layers of lithic clasts (see Fig. 6), some of which sit within impact sags, together indicate a phase of phreatomagmatic activity located within the south crater (e.g., Ross et al., 2017). This phase was characterised by showers of ballistic clasts, dilute ash-rich pyroclastic density currents and ash fall (Fig. 13b). Abundant ash aggregates indicate elevated water vapour in the ash clouds. We interpret these phenomena as the result of phreatomagmatic explosions within an aquifer hosted in lavas and pyroclastic deposits beneath the volcano (Fig. 13). Deposits of unit 1 at distances of ~1 km from the crater on the NW flank of the volcano (Figs. 4e and 6) are characterised by parallel-bedded tuff layers containing ash aggregates and are consistent with fallout from ash clouds generated by discrete phreatomagmatic explosions (e.g, Branney, 1991; Scarpati et al., 1993). Units 2 to 4, composed of ash fall deposits (thin, ash aggregate-bearing tuff beds) and thicker, clast-supported pumice fall deposits with ballistic blocks (Fig. 6), are interpreted as the deposits of alternating phreatomagmatic explosions (ash fall) and magmatic explosions (pumice fall deposits). Bedding in the pumice fall deposits indicates marked unsteadiness in the eruption column, or multiple discrete

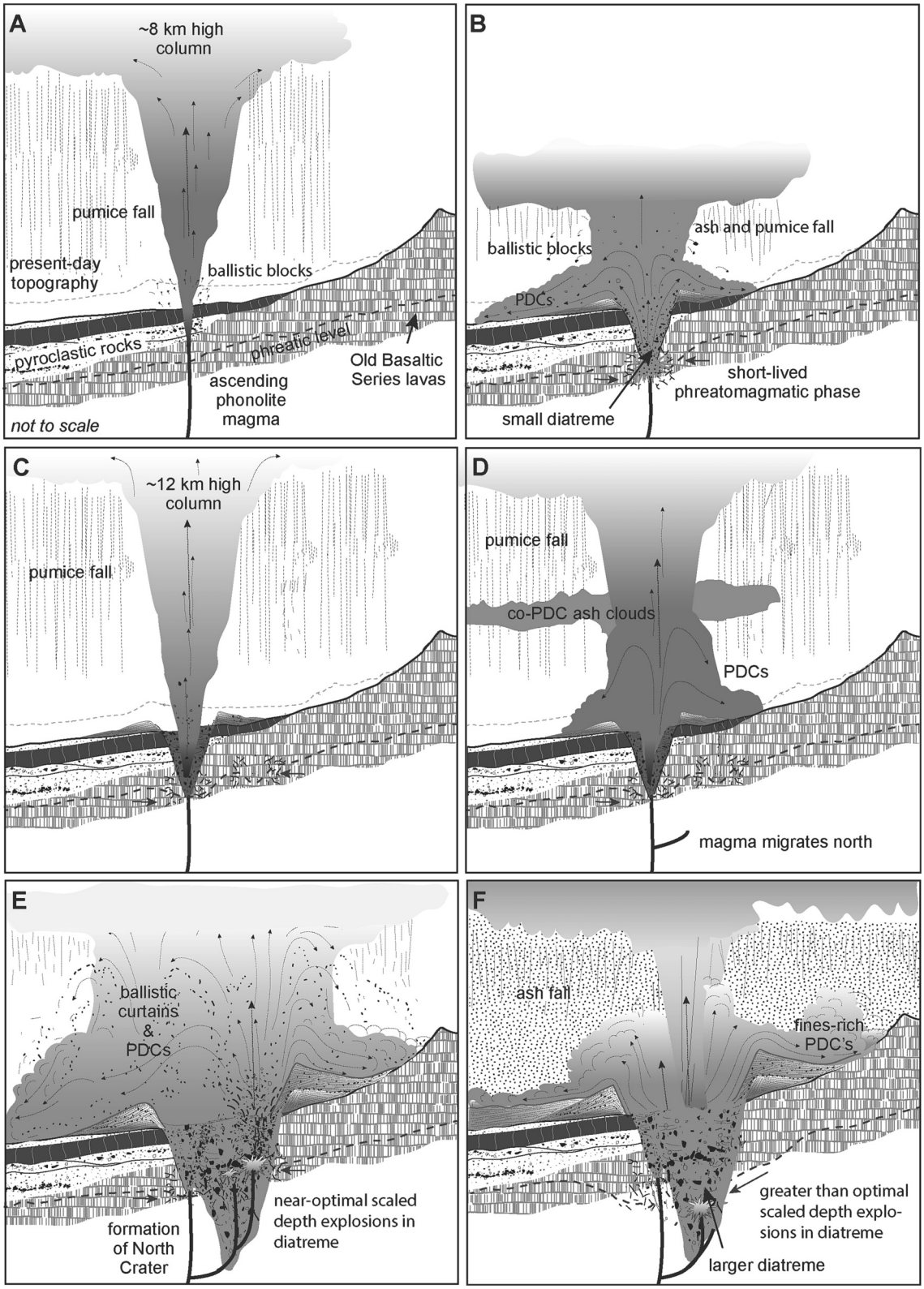

Fig. 13. Conceptual model for the eruption of the Caldera del Rey maar-diatreme volcano. A) Subplinian phase results in an eruption column 8-km-high that disperses tephra towards the west (Member A). B) A brief phreatomagmatic phase, driven by interaction with groundwater generates a small maar-diatreme volcano, and generates short-lived pyroclastic density currents (the south crater) (Member B). C) Migration of magma northwards and second Subplinian phase produces a ~ 12-km-high eruption column which disperses tephra towards the west (Member C). D). Phreatomagmatic phase driven by interaction with groundwater creates a large maar-diatreme volcano (north crater) and results in formation of ballistic curtains, PDCs and ash fall out (Member D). E) Weak and/or deep phreatomagmatic explosions (greater than optimal depth) result in ash-rich explosions and ash-rich PDCs.

explosions.

Member C is lithologically similar to Member A and is interpreted as a pumice fall deposit that records the reestablishment of a Subplinian eruption column that dispersed tephra to the southwest (Fig. 13c). Cross-wind isopleth data (Fig. 5) indicate a column height of ~12.5 km (supplementary information 2). The massive nature of the lower parts of Member C record the fallout of pumice and lithic clasts from a steady eruption column. Thin ash-rich layers may record pauses in the eruption, which allowed ash to settle out, or brief phreatomagmatic explosions, that either punctuated the Subplinian activity or were attendant to it. Elevated lithic clast contents indicate marked erosion of the conduit throughout the Subplinian activity (e.g., Cioni et al., 2015), and the similarity its lithic clast population to Members A and B suggests that it was erupted from the south crater.

The valley-filling beds of massive and bedded lapilli-tuff in Member D that pinch out against paleo-topography (Figs. 4e and 7b) are consistent with deposition from short lived and small-volume PDCs (Fig. 13d) that were dispersed down the north-west flank of the tephra ring in a small paleovalley bordered to the south by the buried Morro Negro ridge (Fig. 1). The interbedded massive pumice and massive tuff beds are interpreted as pumice fall and ash fall deposits. Their presence indicates that PDC generation was intermittent, which is consistent with a Subplinian column that was oscillating between buoyant behaviour and collapsing behaviour. The ash fall deposits are interpreted as co-ignimbrite ash fall deposits that settled out between PDCs. The elevated abundances of welded lapilli tuff clasts in Member D, relative to earlier members, could have resulted from an increase in the excavation depth in the conduit. Alternately, the lapilli-tuff could represent sintered ash, pumice and lithic material that accumulated on the conduit walls and was then subsequently eroded and incorporated into the eruption column.

Member E deposits were emplaced all around the north crater, constructed the bulk of the western flank and draped both sides of Morro Negro (Figs. 1 and 2b) indicating that this phase of the eruption was responsible for the north crater. The proximal deposits consist of couplets of thick beds of massive tuff breccia, with numerous lithic ballistic blocks and impact sags, capped with thin ash aggregate-bearing tuff beds or stratified and cross-stratified lapilli-tuff beds (Fig. 8). This lithological evidence, together with the morphology of the crater and tephra ring (see Figs. 1 and 2a), are consistent with a second phase of phreatomagmatic activity (Fig. 13e).

The couplets are similar to those at other maar-diatreme volcanoes and tuff interpreted as the deposits of either pyroclastic density current deposits or ballistic curtains generated by near-optimal-scaled depth explosions (Valentine et al., 2015; Graettinger and Valentine, 2017; Ort et al., 2018; Valentine et al., 2017; Sweeney et al., 2018). We interpret the coarse-grained lower layers of the couplets as the deposits of ballistic curtains resulting from numerous explosions at depths in the diatreme that formed dense eruptive jets that collapsed as ballistic curtains (e.g., Valentine et al., 2015). The abundant large lithic ballistic clasts and numerous impact sags which strongly disrupt the capping layer of the underlying couplet, support this interpretation. The finer-grained tuff beds and stratified lapilli-tuff beds are interpreted as the deposits of dilute pyroclastic density currents generated in the wake of collapsing ballistic curtains and from ash fall during pauses in phreatomagmatic activity (Fig. 13e) (see Graettinger and Valentine, 2017).

The steep slope to the east acted as a barrier to PDCs and ballistic curtains (cf. Sweeney et al., 2018). The poorly sorted, chaotic deposits of Member E drape the slope but are absent on the ridgeline where the deposits consist instead of parallel-bedded ash fall tuffs and pumice fall deposits with scattered ballistic clasts (Risco Bisechi Fig. 11a). To the west and south, PDCs and ballistic curtains had largely unrestricted pathways to the coast. An upper limit on the runout of PDCs is given by the presence of tephra fall-dominated distal outcrops. These indicate that the PDCs were blocked to the east-northeast by 300 m-high topography and did not flow further than ~2.5 km to the northwest and ~ 4 km to the southeast, although distal, ash-rich deposits of PDC currents can be difficult to distinguish from ash fall deposits (e.g., Brown et al., 2023).

The lithic population in Member E lacks the welded lapilli-tuff and lapilli-stone clasts seem in Members A-C (Fig. 3) and is consistent with a northward shift in vent location to a subsurface region that lacked welded lapilli-tuff (ignimbrite) layers. Alternatively, if the lapilli-tuff clasts represent sintered conduit material, then a northward shift is also required to avoid recycling of welded lapilli-tuff clasts into Member E deposits by phreatomagmatic explosions in the diatreme.

Member F deposits are substantially different to the deposits of Member E. They are fines-rich and lapilli-poor, even in the crater, and contain abundant ash aggregates and evidence for soft-state slumping (Fig. 11). The cross-bedding and lenticular nature of many beds in Member F are indicative of emplacement by dilute, ash-rich PDCs. Ballistic lithic clasts are scarce. These characteristics, along with the strongly bedded nature of the deposits are consistent with an origin via repetitive phreatomagmatic explosions. Member F deposits filled the south crater and the explosions that created them must have occurred within the substantial diatreme generated by the Member E explosions (Fig. 13f). The fine-grained nature of the deposits is compatible with greater-than-optimal scaled depth explosions in a diatreme (Graettinger and Valentine, 2017). Experimental evidence indicates that much of the material involved in such explosions remains trapped at depth (Graettinger et al., 2014) and only fine-grained material escapes to the surface. This ejecta can collapse and produce fine-grained PDCs. We propose that much of Member F was deposited in this way: by fine-grained, mostly dilute PDCs, generated in the north crater and that sedimented material in the south crater and on the tephra ring (now eroded and not preserved).

The lithic population in Member F is dominated by basalt lava lithologies which suggests that explosions for were centred in a basalt-hosted aquifer or within a region of the diatreme that was rich in basalt lithic debris.

5.2. Ash aggregates

The abundance of ash aggregates in the Members B, E and F is strong supporting evidence for phreatomagmatic explosions and for the generation of vapour-rich ash clouds. We infer that aggregation occurred in all fine ash clouds generated during the eruption, and that all fine ash probably accumulated as aggregates of one form or another in both proximal and distal regions (see Durant and Brown, 2016). An association between AP2 aggregates (accretionary lapilli) and PDCs occurs in the deposits of Plinian and Phreatoplinian deposits (Brown et al., 2010; Van Eaton and Wilson, 2013; Hoult et al., 2022), indicating that growth of complexly layered aggregates is triggered by interaction with or passage through PDCs. Simpler AP1 aggregates (ash pellets) are elsewhere limited mainly to ash fall deposits (Brown et al., 2012, 2023). These relationships generally hold true in the CDR deposits, although the locations of aggregate growth and the patterns of deposition are complicated by both the transient nature and the frequency of phreatomagmatic explosions and PDCs, particularly during the emplacement of Member F.

5.3. Vesicularity indices

The vesicularity indices and vesicularity ranges for pumice clast populations varies between the different members. Members A and C, with high indices of 75% and 72%, respectively, and narrow ranges (35%; Fig. 3) are consistent with magmatic eruptions (e.g., Houghton and Wilson, 1989). The lower vesicularity indices of Members B and E (68% and 55%, respectively), their broader ranges (55–60%) and bimodality are consistent with phreatomagmatic eruptions and reflect complex variations in the timing of groundwater-induced fragmentation and vesiculation (e.g., Houghton and Wilson, 1989). The relatively low

vesicularity index of pumice clasts in Member F (57%) and its broad range (75%) and weak bimodality is also indicative of phreatomagmatic activity. We cannot rule out that some of the vesicular clasts in Members C, E and F were recycled in the vent from earlier magmatic phases (e.g., Valentine and White, 2012), but we do not have evidence for this (e.g., ash coatings). Whilst phreatomagmatism is a probable cause of lower vesicularity indices and broad vesicularity ranges (Houghton and Wilson, 1989; White and Valentine, 2016) in the CDR, and is supported by other lithological evidence, we also cannot rule out the role of heterogeneity in mass eruption rates and strongly pulsatory activity, common in Subplinian eruptions, in fragmenting degassed magma and generating pumice clasts with lower vesicularities (Cioni et al., 2015).

5.4. Construction of the CDR maar-diatreme

The CDR eruption initiated when phonolite magma intruded the southern flank of Tenerife and intersected the Earth's surface at ~100 m above present sea level on a shallow slope at the base of the Roque del Conde massif (Fig. 1). Sea level at the time of the eruption was similar to or lower than that of the present day because subaerial CDR ash fall deposits are preserved at present sea level (Fañabe beach, Figs. 1 and 11c).

There are several lines of evidence that indicate that eruptive activity migrated northwards from the south crater to the north crater during the eruption. Limited proximal isopach and isopleth data place the vent for Member A pumice fall deposit in the south crater. Member B is thickest around the south crater and are cut by an inward-dipping scarp in the southern wall of the south crater. We interpret this scarp as the inner crater wall (Fig. 2c), and it suggests that Member B was also erupted from the south crater. Members C is thickest in the south and drapes the south crater wall and the limited isopach and isopleth data do not constrain the location of the vent. Member D forms a substantial tephra ring that is thickest around the north crater (Fig. 2b), and we infer that it too was erupted from the north crater. The marked change in lithic clast population from Member D to Member E is supporting evidence for a change in vent position. The deposits of Member F bank up against the crater wall and fill the south crater (Fig. 1). We attribute the absence of Member E away from the south crater as the result of erosion.

Estimating the true crater size and the original elevation of the crater floor is difficult due to substantial post-eruption erosion. The CDR crater is partially filled with post-eruption volcaniclastic sediments that have been eroded from the surrounding tephra ring, which is almost completely absent on its north side (Fig. 1). We speculate that these sediments are several tens-of-metres thick. Thus, although the crater floor presently sits at around the level of the surrounding pre-eruption ground (~100 m asl; cross-section, Fig. 1), it would have sat below the pre-eruption surface immediately after the eruption. This is consistent with an interpretation as a maar volcano (e.g., Ross et al., 2017), generated by the excavation and expulsion of country rock by phreatomagmatic eruptions within a diatreme.

Member B, erupted from the south crater is not thick, nor apparently widespread, and probably resulted from a short period of phreatomagmatic activity that may not have excavated a substantial diatreme. The thick tephra ring deposits of Member E probably record an extended phreatomagmatic episode that we infer excavated a substantial diatreme beneath the north crater (Fig. 13).

5.5. Transitions between magmatic phases and phreatomagmatic phases

The CDR eruption consisted of two cycles of magmatic-to-phreatomagmatic activity: Members A-B, and Members C—F. The first cycle was focussed in the south crater and the second initiated after magma migrated ~1 km northwest. We found no evidence for a substantial repose period between activity at the south and north craters and we consider that all the deposits of the CDR represent one eruption that may have lasted days-to-months.

The magmatic phases (Members A, C and D) generated Subplinian eruption columns, ~8–12.5 km high, indicative of average mass eruption rates in the region of 10^2–10^3 m^3 s^{-1} (Carey and Sigurdsson, 1989; Mastin et al., 2009). The lithological characteristics of tephra fall deposits in Members A and C, such as bedding defined by changes in grainsize and lithic content, and by thin layers with ash matrices and thin ash layers (Fig. 5), are consistent with Subplinian activity, as the eruption columns are commonly unsteady and may stop and start repeatedly as a function of intermittent magma supply (Bursik, 1993; Cioni et al., 2015). Some ash layers may have resulted from intermittent phreatomagmatic explosions.

Evidence for phreatomagmatism in Members B, E and F includes: (1) The morphology and size of the tephra ring constructed predominantly by Member E deposits. (2) Elevated abundances of shallow lithic clasts sourced from explosions. (3) Abundant ash aggregates that indicate high amounts of water vapour in the erupted mixtures. (4) Numerous ballistic clasts and impact sags. (5) Presence of poorly to incipiently vesicular juvenile clasts (Fig. 3). (6) Lithofacies associations similar to those at other maar-diatreme and tuff ring volcanoes (e.g., massive tuff breccias, cross-stratified tuffs and parallel bedded ash fall deposits, White and Ross, 2011; Ross et al., 2017; Valentine et al., 2017). Whilst no single criterion is diagnostic, a suite of characteristics such as these can be indicative (e.g., White and Valentine, 2016).

Alternations between magmatic and phreatomagmatic activity are recorded in the deposits of many explosive volcanic eruptions and particularly those dominated by phreatomagmatic activity, such as maars and tuff rings (Houghton and Hackett, 1984; Houghton and Schmincke, 1989; Martí et al., 2011; Saucedo et al., 2017). In the latter, these alternations can result from variations in the ascent rates of magma, heterogeneous water distribution or magma ascent pathways within a diatreme, sealing of subsurface permeable fractures by magma or tephra, or in the case of surface magma-water interaction, construction of volcanic edifices that periodically blocks water access to the vent (Valentine and White, 2012; Valentine et al., 2017). Some eruptions started with phreatomagmatic activity and transitioned to effusive activity that emplaced lava flows or domes. or ended with Strombolian activity (Clarke et al., 2009; Zimmer et al., 2010; Austin-Erickson et al., 2011; Kshirsagar et al., 2016), and vice versa (Gutmann, 2002).

Small-volume eruptions of silicic magmas frequently initiate with explosive phases that feed convective columns (Heiken and Wohletz, 1987; Woods and Koyaguchi, 1994; Cassidy et al., 2018). These phases persist until the mass eruption rate is insufficient to support a buoyant column. This can occur due to changes in intrinsic properties such as decreases in magma gas content or magma temperature, or to extrinsic properties, such as increases in vent diameter (Aravena et al., 2017) or vent blockage (Wadsworth et al., 2020). Transitions from explosive to effusive behaviour during silicic eruptions including depletion of gas-rich magma (Popa et al., 2021), in-conduit sintering (Wadsworth et al., 2020), efficient permeable outgassing (Degruyter et al., 2012), and shallow conduit fracturing (Heap et al., 2019).

We attribute transitions from magmatic to phreatomagmatic activity in the CDR eruption to decreases in mass eruption rate which created the conditions suitable for phreatomagmatic activity (see Scandone and Malone, 1985; Houghton and Nairn, 1991; Houghton et al., 1996; Cole et al., 1999; Valentine et al., 2017). During magmatic silicic eruptions, decreases in eruption rate can promote clast capture at conduit walls (Farquharson et al., 2022) and sintering, effectively clogging the vent and constricting the eruptive flow area (e.g., Wadsworth et al., 2020). In turn, this clogging is thought to be coupled to the fragmentation at depth, because a clogged conduit can pressurize, effectively reducing the pressure difference that drives fragmentation (Spieler et al., 2004) and causing a drop in fragmentation efficiency (Kueppers et al., 2006) and waning eruption rate. Waning eruption rates lead to lava effusion (e.g., Cassidy et al., 2018; Wadsworth et al., 2020). During the CDR eruption, lava effusion is not recorded, and we speculate that waning eruption rates (at the end of the phases that deposited Members B and D) instead

lead to phreatomagmatic eruptions due to favourable hydrological conditions: low magma fluxes allowed water to come into contact with ascending phonolitic magma, initiate stress-induced fracturing and trigger phreatomagmatic explosions in a manner similar to that observed in experiments by Austin-Erickson et al. (2011).

5.6. Volume of the CDR eruption and implications for volcanism on Tenerife

The volume of the tephra ring can be estimated by assuming that it originally extended 1 km radially away from the volcano, had a maximum thickness of 70 m, and an average dip of ~4°. This gives a volume of ~1.7×10^8 m^3 (0.17 km^3). Using a nominal average value of of ~20 vol% lithic clasts in the deposits, and assuming a density of 1000 kg/m^3 for the deposit and 2550 kg/m^3 for the magma (Seifert et al., 2013), results in a dense rock equivalent (DRE) volume of ~5.4×10^7 m^3 consistent with typical volumes for silicic lava domes and flows (Fink and Griffiths, 1998).

It is not possible to close isopachs in Members A and C due to dispersal over the sea and to limited onshore outcrops and it difficult to estimate the volume of the Subplinian deposits. Instead, without full justification, we assume that each pumice fall deposit was sub-equal in volume to the tephra ring. This gives a reasonable estimate of ~0.5 km^3 of tephra and we cautiously label it a VEI 4 eruption. For comparison, the preserved volume of the nearby 0.9 Ma phonolite Montaña Guaza dome-flow complex (Hernández-Pacheco et al., 1990; Carracedo et al., 2007; Cas et al., 2022), is ~1 km^3, and phonolite eruptions from the Teide-Pico Viejo-Montana Blanca complex range in volume from 0.01 to 1 km^3 (Martí et al., 2012).

Nearly all eruptions of phonolite magma on Tenerife have occurred either at Las Cañadas caldera (>169 ka, Martí et al., 1994; Ancochea et al., 1999; Brown et al., 2003; Martí, 2019; Davila-Harris et al., 2022), or from the Teide-Pico Viejo-Montaña Blanca composite volcano (<35 ka, Ablay et al., 1998; Carracedo et al., 2003, 2007; Martí et al., 2012). Eruptions from the former have included many Plinian eruptions with DRE volumes >5 km^3 (Bryan et al., 2000; Brown and Branney, 2004; Davila-Harris et al., 2013; Pittari et al., 2006; Edgar et al., 2017). Eruptions from the latter volcano were Subplinian, and generated tephra fall deposits, small-volume PDCs and emplaced lava flows and domes (Ablay et al., 1998; García et al., 2011; Martí et al., 2012).

If the hydrological conditions at the CDR vent site had not been conducive for phreatomagmatic interaction, we speculate that the eruption would have followed a pathway characterised by Subplinian explosive activity alternating with effusion of lava domes/flows. The nearby lava dome-flow complex, Montaña Guaza, 4 km SE of CDR, provides another scenario: an effusion-dominated monogenetic eruption of phonolitic magma (Hernández-Pacheco et al., 1990).

The probability of a similarly located phonolite eruption in the future is remote given that there have been only two phonolite eruptions on the southern flank of Tenerife in the past ~1 Ma. However, Caldera del Rey provides a useful case study on how such eruptions could proceed where both environmental and eruptive conditions are conducive to phreatomagmatic activity.

6. Conclusions

The phonolitic Caldera del Rey nested maar volcano in southern Tenerife, Canary Islands, is a superb example of the deposits of a strongly water-modified monogenetic silicic eruption. The VEI ~ 4 eruption commenced with a Subplinian phase that resulted in an 8 km-high eruption column that dispersed tephra west of the volcano. This transitioned into a short-lived phreatomagmatic phase, before the eruption resumed Subplinian activity that fed a > 12 km-high plume, showered out pumice and ended with the generation intermittent PDCs alongside tephra fall. Migration of magma northwards resulted in phreatomagmatic activity and the formation of a substantial tephra ring and the excavation of a diatreme beneath the north crater. The bulk of the tephra ring resulted from near-optimal-scaled depth (shallow and or strong) explosions that generated successive ballistic curtains and PDCs. Over time explosions transitioned to greater-than-optimal scaled depth (deep and or weak) ejected predominantly fine-grained material dispersed by PDCs. During the phreatomagmatic phases substantial thickness of ash accumulated at distances exceeding a few kilometres from the vent. The CDR eruption provides a useful case study for understanding the deposits and hazards associated with phreatomagmatic eruptions involving silicic magma.

CRediT authorship contribution statement

Oliver Bowers: Investigation, Writing – original draft. **Pablo Dávila-Harris:** Conceptualization, Investigation, Writing – review & editing. **Rebecca Winstanley:** Investigation, Writing – review & editing. **Fabian B. Wadsworth:** Writing – review & editing. **Richard J. Brown:** Conceptualization, Funding acquisition, Project administration, Investigation, Writing – review & editing.

Declaration of Competing Interest

The authors declare that they have no known competing financial interests or personal relationships that could have appeared to influence the work reported in this paper.

Data availability

Data will be made available on request.

Acknowledgements

We thank Alexis Schwartz for support in the field. Ed Llewellin and Rebecca Williams provided helpful comments on the thesis that this paper is based on. We thank Leon Bowen for help and support. Alison Graettinger and Rafaello Cioni are thanked for detailed and constructive reviews.

Appendix A. Supplementary data

Supplementary data to this article can be found online at https://doi.org/10.1016/j.jvolgeores.2023.107920.

References

Ablay, G.J., Carroll, M.R., Palmer, M.R., Martí, J., Sparks, R.S., 1998 May 1. Basanite–phonolite lineages of the Teide–Pico Viejo volcanic complex, Tenerife, Canary Islands. J. Petrol. 39 (5), 905–936.

Ancochea, E., Huertas, M.J., Cantagrel, J.M., Coello, J., Fúster, J.M., Arnaud, N., Ibarrola, E., 1999. Evolution of the Cañadas edifice and its implications for the origin of the Cañadas Caldera (Tenerife, Canary Islands). J. Volcanol. Geotherm. Res. 88 (3), 177–199.

Aravena, Á., Vitturi, M.D.M., Cioni, R., Neri, A., 2017. Stability of volcanic conduits during explosive eruptions. J. Volcanol. Geotherm. Res. 339, 52–62.

Austin-Erickson, A., Büttner, R., Dellino, P., Ort, M.H., Zimanowski, B., 2008. Phreatomagmatic explosions of rhyolitic magma: experimental and field evidence. J. Geophys. Res. 113 paper B11201.

Austin-Erickson, A., Ort, M.H., Carrasco-Núñez, G., 2011. Rhyolitic phreatomagmatism explored: Tepexitl tuff ring (Eastern Mexican Volcanic Belt). J. Volcanol. Geotherm. Res. 201, 325–341.

Aziwo, B.T., Tamen, J., Chako-Tchamabé, B., Asaah, A.N.E., Kimoun-Yangouo, F., Zemfack-Dongmo, B.S., Tedonkenfack, S.S.T., 2022. Tephrostratigraphy and morphometry of Wum Maar Volcano (Oku Volcanic Group-Cameroon Volcanic line): implications for complex monogenetic volcanoes. J. Afr. Earth Sci. 188, 104470.

Biass, S., Bagheri, G., Bonadonna, C., 2015. A Matlab Implementation of the Carey and Sparks (1986) Model to Estimate Column Height and Wind Speed from Isopleth Maps. Department of Earth Sciences, University of Geneva, Switzerland.

Bonadonna, C., Cioni, R., Pistolesi, M., Connor, C., Scollo, S., Pioli, L., Rosi, M., 2013. Determination of the largest clast sizes of tephra deposits for the characterization of explosive eruptions: a study of the IAVCEI commission on tephra hazard modelling. Bull. Volcanol. 75, 1–15. https://doi.org/10.1007/s00445-012-0680-3.

Branney, M.J., 1991. Eruption and depositional facies of the Whorneyside tuff formation, English Lake District: an exceptionally large-magnitude phreatoplinian eruption. Geol. Soc. Am. Bull. 103 (7), 886–897.
Branney, M.J., Kokelaar, P., 2002. Sedimentation of Ignimbrites from Pyroclastic Density Currents. Special Publication of the Geological Society, London.
Brooker, M.R., Houghton, B.F., Wilson, C.J.N., Gamble, J.A., 1993. Pyroclastic phases of a rhyolitic dome-building eruption: Puketarata tuff ring, Taupo Volcanic Zone, New Zealand. Bull. Volcanol. 55, 395–406.
Brown, R.J., Branney, M.J., 2004. Event-stratigraphy of a caldera-forming ignimbrite eruption on Tenerife: the 273 ka Poris formation. Bull. Volcanol. 66 (5), 392–416.
Brown, R.J., Branney, M.J., 2013. Internal flow variations and diachronous sedimentation within extensive, sustained, density-stratified pyroclastic density currents flowing down gentle slopes, as revealed by the internal architectures of ignimbrites on Tenerife. Bull. Volcanol. 75 (7), 1–24.
Brown, R.J., Valentine, G.A., 2013. Physical characteristics of kimberlite and basaltic intraplate volcanism and implications of a biased kimberlite record. Bulletin 125 (7–8), 1224–1238.
Brown, R.J., Barry, T.L., Branney, M.J., Pringle, M.S., Bryan, S.E., 2003. The Quaternary pyroclastic succession of southern Tenerife, Canary Islands: explosive eruptions, related caldera subsidence and sector collapse. Geol. Mag. 140, 265–288.
Brown, R.J., Kokelaar, B.P., Branney, M.J., 2007. Widespread transport of pyroclastic density currents from a large silicic tuff ring: the Glaramara tuff, Scafell caldera, English Lake District, UK. Sedimentology 54, 1163–1189.
Brown, R., Branney, M., Maher, C., Davila-Harris, P., 2010. Origin of accretionary lapilli within ground-hugging density currents: evidence from pyroclastic couplets on Tenerife. GSA Bull. 122 (1–2), 305–320.
Brown, R.J., Bonadonna, C., Durant, A.J., 2012. A review of volcanic ash aggregation. Phys. Chem. Earth A/B/C 45 (2012), 65–78.
Brown, R.J., Van Eaton, A.R., Hernández, W., Condren, P., Sweeney, C., Tournigand, P. Y., Vallance, J.W., 2023. Ash aggregate-rich pyroclastic density currents of the 431 CE Tierra Blanca Joven eruption, Ilopango caldera, El Salvador. J. Volcanol. Geotherm. Res. 107845.
Bryan, S.E., Martí, J., Cas, R.A.F., 1998. Stratigraphy of the Bandas del Sur formation: an extracaldera record of Quaternary phonolitic explosive volcanism from the Las Cañadas edifice, Tenerife (Canary Islands). Geol. Mag. 135, 605–636.
Bryan, S.E., Cas, R.A.F., Martı, J., 2000. The 0.57 Ma plinian eruption of the Granadilla Member, Tenerife (Canary Islands): an example of complexity in eruption dynamics and evolution. J. Volcanol. Geotherm. Res. 103 (1–4), 209–238.
Bursik, M., 1993 Sep 1. Subplinian eruption mechanisms inferred from volatile and clast dispersal data. J. Volcanol. Geotherm. Res. 57 (1–2), 57–70.
Cano-Cruz, M., Carrasco-Núñez, G., 2008. Evolution of a rhyolitic explosion crater (maar): Hoya de Estrada, Valle de Santiago volcanic field, Guanajuato, Mexico. Revista Mexicana de Ciencias Geologicas 25, 549–564.
Carey, S., Sigurdsson, H., 1989. The intensity of plinian eruptions. Bull. Volcanol. 51 (1), 28–40.
Carey, S., Sparks, R.S.J., 1986. Quantitative models of the fallout and dispersal of tephra from volcanic eruption columns. Bull. Volcanol. 48 (2), 109–125.
Carmona, J., Romero, C., Dóniz, J., García, A., 2011. Characterization and facies analysis of the hydrovolcanic deposits of Montaña Pelada tuff ring: Tenerife, Canary Islands. J. Afr. Earth Sci. 59 (1), 41–50.
Carracedo, J.C., Paterne, M., Guillou, H., Perez-Torrado, F.J., Paris, R.M., Rodriguez-Badiola, E., Hansen Machín, A.R., 2003. Dataciones radiométricas (14C y K/Ar) del Teide y el rift noroeste, Tenerife, Islas Canarias. Estud 59, 15–29.
Carracedo, J.C., Badiola, E.R., Guillou, H., Paterne, M., Scaillet, S., Torrado, F.P., Paris, R., Fra-Paleo, U., Hansen, A., 2007 Sep 1. Eruptive and structural history of Teide Volcano and rift zones of Tenerife, Canary Islands. Geol. Soc. Am. Bull. 119 (9–10), 1027–1051.
Carrasco-Núñez, G., Ort, M., Romero, C., 2007. Evolution and hydrological conditions of a maar volcano (Atexcac crater, Eastern Mexico). J. Volcanol. Geotherm. Res. 159, 179–197.
Cas, R.A., Wolff, J.A., Marti, J., Olin, P.H., Edgar, C.J., Pittari, A., Simmons, J.M., 2022. Tenerife, a complex end member of basaltic oceanic island volcanoes, with explosive polygenetic phonolitic calderas, and phonolitic-basaltic stratovolcanoes. Earth Sci. Rev. 230, 103990.
Cassidy, M., Manga, M., Cashman, K., Bachmann, O., 2018. Controls on explosive-effusive volcanic eruption styles. Nat. Commun. 9 (1), 1–16.
Chough, S.K., Sohn, Y.K., 1990. Depositional mechanics and sequences of base surges, Songaksan tuff ring, Cheju Island, Korea. Sedimentology 37, 1115–1135.
Cioni, R., Pistolesi, M., Rosi, M., 2015. Plinian and subplinian eruptions. In: The Encyclopedia of Volcanoes. Academic Press, pp. 519–535.
Clarke, H., Troll, V.R., Carracedo, J.C., 2009 Mar 10. Phreatomagmatic to strombolian eruptive activity of basaltic cinder cones: Montana Los Erales, Tenerife, Canary Islands. J. Volcanol. Geotherm. Res. 180 (2–4), 225–245.
Cole, P.D., Guest, J.E., Queiroz, G., Wallenstein, N., Pacheco, J.M., Gaspar, J.L., Ferreira, T., Duncan, A.M., 1999 Sep 1. Styles of volcanism and volcanic hazards on Furnas volcano, Sao Miguel, Azores. J. Volcanol. Geotherm. Res. 92 (1–2), 39–53.
Cole, P.D., Guest, J.E., Duncan, A.M., Pacheco, J.M., 2001 Jun. Capelinhos 1957–1958, Faial, Azores: deposits formed by an emergent surtseyan eruption. Bull. Volcanol. 63 (2), 204–220.
Davila-Harris, P., 2011. Explosive Ocean-Island Volcanism: The 1.8–0.7 Ma Explosive Eruption History of Cañadas Volcano Recorded by the Pyroclastic Successions Around Adeje and Abona, Southern Tenerife, Canary Islands. Unpublished PhD thesis. University of Leicester.
Davila-Harris, P., Ellis, B.S., Branney, M.J., Carrasco-Núñez, G., 2013. Lithostratigraphic analysis and geochemistry of a vitric spatter-bearing ignimbrite: the Quaternary Adeje formation, Cañadas volcano, Tenerife. Bull. Volcanol. 75 (6), 1–15.
Davila-Harris, P., Branney, M.J., Storey, M., Taylor, R.N., Sliwinski, J.T., 2022. The upper Pleistocene (1.8-0.7 Ma) explosive eruptive history of Las Cañadas volcano, Tenerife: pyroclastic succession of Plinian-ignimbrite eruptions at an ocean-island volcano. J. Volcanol. Geotherm. Res. 436, 107777.
De La Nuez, J., Alonso, J., Quesada, M., Macau, M.D., 1993. Edificios hidromagmáticos costeros de Tenerife (Islas Canarias). Rev. Soc. Geol. Esp. 6, 47–59.
Degruyter, W., Bachmann, O., Burgisser, A., Manga, M., 2012. The effects of outgassing on the transition between effusive and explosive silicic eruptions. Earth Planet. Sci. Lett. 349, 161–170.
Durant, A.J., Brown, R.J., 2016. Ash aggregation in volcanic clouds. In: Volcanic Ash. Elsevier, pp. 53–65.
Edgar, C.J., Wolff, J.A., Olin, P.H., Nichols, H.J., Pittari, A., Cas, R.A.F., Reiners, P.W., Spell, T.L., Martí, J., 2007. The late Quaternary Diego Hernandez formation, Tenerife: volcanology of a complex cycle of voluminous explosive phonolitic eruptions. J. Volcanol. Geotherm. Res. 160 (1–2), 59–85.
Edgar, C.J., Cas, R.A., Olin, P.H., Wolff, J.A., Martí, J., Simmons, J.M., 2017. Causes of complexity in a fallout dominated plinian eruption sequence: 312 ka Fasnia Member, Diego Hernández formation, Tenerife, Spain. J. Volcanol. Geotherm. Res. 345, 21–45.
El Messbahi, H., Dautria, J.M., Jourde, H., Munch, P., Alard, O., Bodinier, J.L., Ouali, H., 2020. Eruption dynamics of pleistocene maars and tuff rings from the Azrou-Timahdite district (Middle Atlas, northern Morocco) and its relevance to environmental changes and ground water table characteristics. J. Afr. Earth Sci. 167, 103845.
Farquharson, J.I., Tuffen, H., Wadsworth, F.B., Castro, J.M., Unwin, H., Schipper, C.I., 2022. In-conduit capture of sub-micron volcanic ash particles via turbophoresis and sintering. Nat. Commun. 13 (1), 1–11.
Fink, J.H., Griffiths, R.W., 1998 Jan 10. Morphology, eruption rates, and rheology of lava domes: insights from laboratory models. J. Geophys. Res. Solid Earth 103 (B1), 527–545.
Freda, C., Gaeta, M., Karner, D.B., Marra, F., Renne, P., Taddeucci, J., Scarlato, P., Christensen, J.N., Dallai, L., 2005. Eruptive history and petrologic evolution of the Albano multiple maar (Alban Hills, Central Italy). Bull. Volcanol. 68, 567–591.
García, O., Martí, J., Aguirre, G., Geyer, A., Iribarren, I., 2011 Jun. Pyroclastic density currents from Teide–Pico Viejo (Tenerife, Canary Islands): implications for hazard assessment. Terra Nova 23 (3), 220–224.
Goto, A., Taniguchi, H., Yoshida, M., Ohba, T., Oshima, H., 2001. Effects of explosion energy and depth to the formation of blast wave and crater: field explosion experiment for the understanding of volcanic explosion. Geophys. Res. Lett. 28 (22), 4287–4290.
Graettinger, A.H., 2018. Trends in maar crater size and shape using the global Maar volcano location and shape (MaarVLS) database. J. Volcanol. Geotherm. Res. 357, 1–13.
Graettinger, A.H., Valentine, G.A., 2017. Evidence for the relative depths and energies of phreatomagmatic explosions recorded in tephra rings. Bull. Volcanol. 79 (12), 1–21.
Graettinger, A.H., Valentine, G.A., Sonder, I., Ross, P.S., White, J.D., Taddeucci, J., 2014. Maar-diatreme geometry and deposits: subsurface blast experiments with variable explosion depth. Geochem. Geophys. Geosyst. 15 (3), 740–764.
Graettinger, A.H., Valentine, G.A., Sonder, I., Ross, P.S., White, J.D., 2015. Facies distribution of ejecta in analog tephra rings from experiments with single and multiple subsurface explosions. Bull. Volcanol. 77 (8), 1–12.
Gutmann, J.T., 2002 Mar 15. Strombolian and effusive activity as precursors to phreatomagmatism: eruptive sequence at maars of the Pinacate volcanic field, Sonora, Mexico. J. Volcanol. Geotherm. Res. 113 (1–2), 345–356.
Heap, M.J., Tuffen, H., Wadsworth, F.B., Reuschlé, T., Castro, J.M., Schipper, C.I., 2019. The permeability evolution of tuffisites and implications for outgassing through dense rhyolitic magma. J. Geophys. Res. Solid Earth 124 (8), 8281–8299.
Heiken, G.H., Wohletz, K., 1987. Tephra deposits associated with silicic domes and lava flows. Geol. Soc. Am. Spec. Pap. 212, 55–76.
Hernández, J.G., Notario del Pino, J.S., Gonzalez Martin, M.M., Hernan Reguera, F., Rodriguez Losada, J.A., 1993. Zeolites in pyroclastic deposits in southeastern Tenerife (Canary Islands). Clay Clay Miner. 41, 521–526.
Hernández-Pacheco, A., De la Nuez, J., Cubas, C.R., Hernán, F., Fernández, S., 1990 Aug 30. Los Domos sálicos de Tenerife, Islas Canarias. Estud. Geol. 46 (3–4), 175–184.
Houghton, B.F., Hackett, W.R., 1984 Aug 1. Strombolian and phreatomagmatic deposits of Ohakune Craters, Ruapehu, New Zealand: a complex interaction between external water and rising basaltic magma. J. Volcanol. Geotherm. Res. 21 (3–4), 207–231.
Houghton, B.F., Nairn, I.A., 1991. The 1976–1982 Strombolian and phreatomagmatic eruptions of White Island, New Zealand – eruptive and depositional mechanisms at a wet volcano. Bull. Volcanol. 54, 25–49.
Houghton, B.F., Schmincke, H.U., 1989. Rothenberg scoria cone, East Eifel: a complex Strombolian and phreatomagmatic volcano. Bull. Volcanol. 52 (1), 28–48.
Houghton, B.F., Wilson, C.J.N., 1989. A vesicularity index for pyroclastic deposits. Bull. Volcanol. 51, 451–462.
Houghton, B.F., Wilson, C.J.N., Rosenberg, M.D., Smith, I.E.M., Parker, R.J., 1996. Mixed deposits of complex magmatic and phreatomagmatic volcanism: an example from Crater Hill, Auckland, New Zealand. Bull. Volcanol. 58, 59–66.
Hoult, H., Brown, R.J., Van Eaton, A.R., Hernandez, W., Dobson, K.J., Woodward, B., 2022. Growth of complex volcanic ash aggregates in the Tierra Blanca Joven eruption of Ilopango Caldera, El Salvador. J. Volcanol. Geotherm. Res. 431, 107670.
Houser, F.N., 1969. Subsidence related to underground nuclear explosions, Nevada Test Site. Bull. Seismol. Soc. Am. 59 (6), 2231–2251.
Kienle, J., Kyle, P.R., Self, S., Motyka, R.J., Lorenz, V., 1980. Ukinrek maars, Alaska, 1. April 1977 eruption sequence, petrology and tectonic setting. J. Volcanol. Geotherm. Res. 7, 11–37.

Kokelaar, B.P., 1983. The mechanism of Surtseyan volcanism. J. Geol. Soc. Lond. 140, 939–944.
Kshirsagar, P., Siebe, C., Guilbaud, M.N., Salinas, S., 2016 May 15. Geological and environmental controls on the change of eruptive style (phreatomagmatic to Strombolian-effusive) of Late Pleistocene El Caracol tuff cone and its comparison with adjacent volcanoes around the Zacapu basin (Michoacán, México). J. Volcanol. Geotherm. Res. 318, 114–133.
Kueppers, U., Scheu, B., Spieler, O., Dingwell, D.B., 2006. Fragmentation efficiency of explosive volcanic eruptions: a study of experimentally generated pyroclasts. J. Volcanol. Geotherm. Res. 153 (1–2), 125–135.
Lorenz, V., 1986. On the growth of maars and diatremes and its relevance to the formation of tuff rings. Bull. Volcanol. 48 (5), 265–274.
Martí, J., 2019. Las Cañadas caldera, Tenerife, Canary Islands: a review, or the end of a long volcanological controversy. Earth Sci. Rev. 196, 102889.
Martí, J., Mitjavila, J., Araña, V., 1994. Stratigraphy, structure and geochronology of the Las Cañadas caldera (Tenerife, Canary Islands). Geol. Mag. 131, 715–727.
Martí, J., Planagumà, L., Geyer, A., Canal, E., Pedrazzi, D., 2011 Apr 15. Complex interaction between Strombolian and phreatomagmatic eruptions in the Quaternary monogenetic volcanism of the Catalan Volcanic Zone (NE of Spain). J. Volcanol. Geotherm. Res. 201 (1–4), 178–193.
Martí, J., Sobradelo, R., Felpeto, A., García, O., 2012 Apr. Eruptive scenarios of phonolitic volcanism at Teide–Pico Viejo volcanic complex (Tenerife, Canary Islands). Bull. Volcanol. 74 (3), 767–782.
Mastin, L.G., Guffanti, M., Servranckx, R., Webley, P., Barsotti, S., Dean, K., Durant, A., Ewert, J.W., Neri, A., Rose, W.I., Schneider, D., 2009. A multidisciplinary effort to assign realistic source parameters to models of volcanic ash-cloud transport and dispersion during eruptions. J. Volcanol. Geotherm. Res. 186 (1–2), 10–21.
McClintock, M., White, J.D., 2006. Large phreatomagmatic vent complex at Coombs Hills, Antarctica: wet, explosive initiation of flood basalt volcanism in the Ferrar-Karoo LIP. Bull. Volcanol. 68 (3), 215–239.
Monsalve, M.L., Martin, I.D.O., Vallejo, H.A., 2023. Morphology and general stratigraphy of the maar-type San Diego volcano, NE of Caldas, Colombia. Boletín Geológico 50 (1).
Ort, M.H., Lefebvre, N.S., Neal, C.A., McConnell, V.S., Wohletz, K.H., 2018. Linking the Ukinrek 1977 maar-eruption observations to the tephra deposits: new insights into maar depositional processes. J. Volcanol. Geotherm. Res. 360, 36–60.
Paradas Herrero, A., Fernandez Santín, S., 1984. Estudio vulcanológico y geoquímico del maar de la CDR, Tenerife (Canarias). Estud. Geol. 40, 285–313.
Pittari, A., Cas, R.A.F., Edgar, C.J., Nichols, H.J., Wolff, J.A., Martí, J., 2006. The influence of palaeotopography on facies architecture and pyroclastic flow processes of a lithic-rich ignimbrite in a high gradient setting: the Abrigo Ignimbrite, Tenerife, Canary Islands. J. Volcanol. Geotherm. Res. 152 (3–4), 273–315.
Popa, R.G., Bachmann, O., Huber, C., 2021. Explosive or effusive style of volcanic eruption determined by magma storage conditions. Nat. Geosci. 14 (10), 781–786.
Ross, P.-S., Carrasco-Núñez, G., Hayman, P., 2017. Felsic maar-diatreme volcanoes: a review. Bull. Volcanol. 79, 1–33. Article 20.
Saucedo, R., Macías, J.L., Ocampo-Díaz, Y.Z.E., Gómez-Villa, W., Rivera-Olguín, E., Castro-Govea, R., Sánchez-Núñez, J.M., Layer, P.W., Hernández, J.T., Carrasco-Núñez, G., 2017. Mixed magmatic–phreatomagmatic explosions during the formation of the Joya Honda maar, San Luis Potosí, Mexico. Geol. Soc. Lond. Spec. Publ. 446 (1), 255–279.
Scandone, R., Malone, S.D., 1985 Feb 1. Magma supply, magma discharge and readjustment of the feeding system of Mount St. Helens during 1980. J. Volcanol. Geotherm. Res. 23 (3–4), 239–262.
Scarpati, C., Cole, P., Perrotta, A., 1993. The Neapolitan Yellow Tuff—a large volume multiphase eruption from Campi Flegrei, southern Italy. Bull. Volcanol. 55, 343–356.
Seifert, R., Malfait, W.J., Petitgirard, S., Sanchez-Valle, C., 2013 Nov 1. Density of phonolitic magmas and time scales of crystal fractionation in magma chambers. Earth Planet. Sci. Lett. 381, 12–20.
Sieh, K., Bursik, M., 1986. Most recent eruption of the Mono Craters, eastern Central California. J. Geophys. Res. Solid Earth 91 (B12), 12539–12571.
Sohn, Y.K., 1996. Hydrovolcanic processes forming basaltic tuff rings and cones on Cheju Island, Korea. Geol. Soc. Am. Bull. 108, 1199–1211.
Sohn, Y.K., Chough, S.K., 1989. Depositional processes of the Suwolbong tuff ring, Cheju Island (Korea). Sedimentology 40, 837–855.
Solgevik, H., Mattsson, H.B., Hermelin, O., 2007 Jan 1. Growth of an emergent tuff cone: fragmentation and depositional processes recorded in the Capelas tuff cone, São Miguel, Azores. J. Volcanol. Geotherm. Res. 159 (1–3), 246–266.
Sonder, I., Graettinger, A.H., Valentine, G.A., 2015. Scaling multiblast craters: general approach and application to volcanic craters. J. Geophys. Res. Solid Earth 120 (9), 6141–6158.
Spieler, O., Kennedy, B., Kueppers, U., Dingwell, D.B., Scheu, B., Taddeucci, J., 2004. The fragmentation threshold of pyroclastic rocks. Earth Planet. Sci. Lett. 226 (1–2), 139–148.
Sweeney, M.R., Grosso, Z.S., Valentine, G.A., 2018. Topographic controls on a phreatomagmatic maar-diatreme eruption: field and numerical results from the Holocene Dotsero volcano (Colorado, USA). Bull. Volcanol. 80 (11), 1–25.
Tait, M.A., Cas, R.A.F., Viramonte, J.G., 2009. The origin of an unusual tuff ring of perlitic rhyolite pyroclasts: the last explosive phase of the Ramadas Volcanic Centre, Andean Puna, Salta, NW Argentina. J. Volcanol. Geotherm. Res. 1 (183), 1–16.
Tchamabé, B.C., Carrasco-Núñez, G., Miggins, D.P., Németh, K., 2020. Late Pleistocene to Holocene activity of Alchichica Maar volcano, eastern trans-Mexican volcanic belt. J. S. Am. Earth Sci. 97, 102404.
Valentine, G.A., White, J.D.L., 2012. Revised conceptual model for maar-diatremes: subsurface processes, energetics, and eruptive products. Geology 40, 1111–1114.
Valentine, G.A., Graettinger, A.H., Sonder, I., 2014. Explosion depths for phreatomagmatic eruptions. Geophys. Res. Lett. 41 (9), 3045–3051.
Valentine, G.A., Graettinger, A.H., Macorps, É., Ross, P.S., White, J.D., Döhring, E., Sonder, I., 2015. Experiments with vertically and laterally migrating subsurface explosions with applications to the geology of phreatomagmatic and hydrothermal explosion craters and diatremes. Bull. Volcanol. 77 (3), 1–17.
Valentine, G.A., White, J.D.L., Ross, P.-S., Graettinger, A.H., Sonder, I., 2017. Updates to concepts on phreatomagmatic Maar-diatremes and their pyroclastic deposits. Front. Earth Sci. 5, 68.
Valentine, G.A., Fierstein, J., White, J.D., 2022. Pyroclastic deposits of Ubehebe Crater, Death Valley, California, USA: ballistics, pyroclastic surges, and dry granular flows. Geospher 18, 1926–1957.
Van Eaton, A.R., Wilson, C.J., 2013. The nature, origins and distribution of ash aggregates in a large-scale wet eruption deposit: Oruanui, New Zealand. J. Volcanol. Geotherm. Res. 250, 129–154.
Wadsworth, F.B., Llewellin, E.W., Vasseur, J., Gardner, J.E., Tuffen, H., 2020. Explosive-effusive volcanic eruption transitions caused by sintering. Sci. Adv. 6 (39) eaba7940.
White, J.D.L., 1991. Maar-diatreme phreatomagmatism at Hopi Buttes, Navajo Nation (Arizona), USA. Bull. Volcanol. 53, 239–258.
White, J.D.L., Ross, P.-S., 2011. Maar-diatreme volcanoes: a review. J. Volcanol. Geotherm. Res. 201, 1–29.
White, J.D., Valentine, G.A., 2016. Magmatic versus phreatomagmatic fragmentation: absence of evidence is not evidence of absence. Geosphere 12 (5), 1478–1488.
Wohletz, K., Heiken, G., 1992. Volcanology and Geothermal Energy, vol. 432. University of California Press, Berkeley.
Woods, A.W., Koyaguchi, T., 1994. Transitions between explosive and effusive eruptions of silicic magmas. Nature 370 (6491), 641–644.
Zimmer, B.W., Riggs, N.R., Carrasco-Núñez, G., 2010. Evolution of tuff ring-dome complex: the case study of Cerro Pinto, eastern Trans-Mexican Volcanic Belt. Bull. Volcanol. 72 (10), 1223–1240.